minerals

MDPI

Article

Zircon U-Pb and Fission-Track Chronology of the Kaiyang Phosphate Deposit in the Yangtze Block: Implications for the Rodinia Supercontinent Splitting and Subsequent Thermal Events

Yina Song [1], Tianqi Li [1], Jiayi Zhou [1], Debin Zhu [2] and Lingling Xiao [1,*]

[1] School of Civil and Resource Engineering, University of Science and Technology Beijing, Beijing 100083, China; songyina1999@aliyun.com (Y.S.); m202210009@xs.ustb.edu.cn (T.L.); m202310020@xs.ustb.edu.cn (J.Z.)
[2] Institute of Regional Geological Survey Guizhou Province, Guiyang 550300, China; debinzhu0605@163.com
* Correspondence: x_lingling@126.com

Abstract: The Kaiyang phosphate mining area in Guizhou, which is located in the central–southern part of the Yangtze Block, hosts one of China's more significant phosphate-enriched strata within the Doushantuo Formation. This formation is essential for phosphate mining and also preserves multiple magmatic events, which are closely linked to the assembly and breakup of the Rodinia supercontinent. Our comprehensive studies in petrology, geochemistry, zircon U-Pb geochronology, and fission-track dating reveal that the primary ore mineral in phosphorite is collophane, which is accompanied by dolomite, quartz, pyrite, and zircon. The majority of detrital zircons in the phosphorite, as well as the overlying dolostone and underlying sandstone, are of magmatic origin, with a record of multiple stages of magmatic ages. Among these, the older age groups of ~2500 Ma and ~2000–1800 Ma represent the ancient crystalline basement of the Yangtze Block from the Paleoproterozoic era. The three main age peaks at ~880 Ma, ~820 Ma, and ~780 Ma indicate that the magmatic event at ~880 Ma was related to the assembly of the Rodinia supercontinent during the Grenvillian period. The most prominent age peak at ~820 Ma marks a critical time point for the transition from assembly to the breakup of the Rodinia supercontinent, with the Yangtze Block's response to the supercontinent breakup events lasting at least until ~780 Ma. The youngest group of zircon ages from the phosphorite (~594 Ma), and the underlying sandstone (~529 Ma) establishes the minimum age for the phosphorite formation, indicating that the Doushantuo phosphorite layer in the Kaiyang area was formed after 594 Ma, i.e., even later than 529 Ma. The zircon fission-track ages in the three rock types of the phosphorite-bearing rocks can be divided into three groups: 501–489 Ma, ~366 Ma, and 53–39 Ma. All of these groups are presumed to be associated with the tectonic uplift events that follow mineralization. The first two age groups correspond to the two major tectonic uplift events during the Caledonian period, which resulted in the formation of the Qianzhong Uplift. The ages of 53–39 Ma are related to the late uplift of the Himalayan orogeny, and they represent its response in the Kaiyang area of Guizhou.

Keywords: Rodinia supercontinent breakup; Doushantuo Formation; phosphorite; zircon LA-ICP-MS; zircon fission track

Citation: Song, Y.; Li, T.; Zhou, J.; Zhu, D.; Xiao, L. Zircon U-Pb and Fission-Track Chronology of the Kaiyang Phosphate Deposit in the Yangtze Block: Implications for the Rodinia Supercontinent Splitting and Subsequent Thermal Events. *Minerals* **2024**, *14*, 585. https://doi.org/10.3390/min14060585

Academic Editor: Jim Lee

Received: 3 April 2024
Revised: 27 May 2024
Accepted: 30 May 2024
Published: 31 May 2024

1. Introduction

"Rodinia" refers to a supercontinent that existed during the late Mesoproterozoic to the early Neoproterozoic era, but its geographical boundaries and precise evolutionary timelines are still undetermined. Consequently, there is ongoing debate regarding the timing of Rodinia's assembly and breakup. It is generally believed that, around 820 Ma, Rodinia transitioned from a phase of amalgamation to fragmentation. The breakdown of the supercontinent involved multiple distinct phases and stages [1–3]. The Yangtze Block,

a significant component of China's Precambrian crust [4,5], was once part of Rodinia and thus offers crucial insights into the supercontinent's evolutionary history. Previous isotopic geochronology studies on various Precambrian rock types exposed in the Yangtze Block (Figure 1) provide essential scientific data for clarifying the complete evolutionary history of Rodinia.

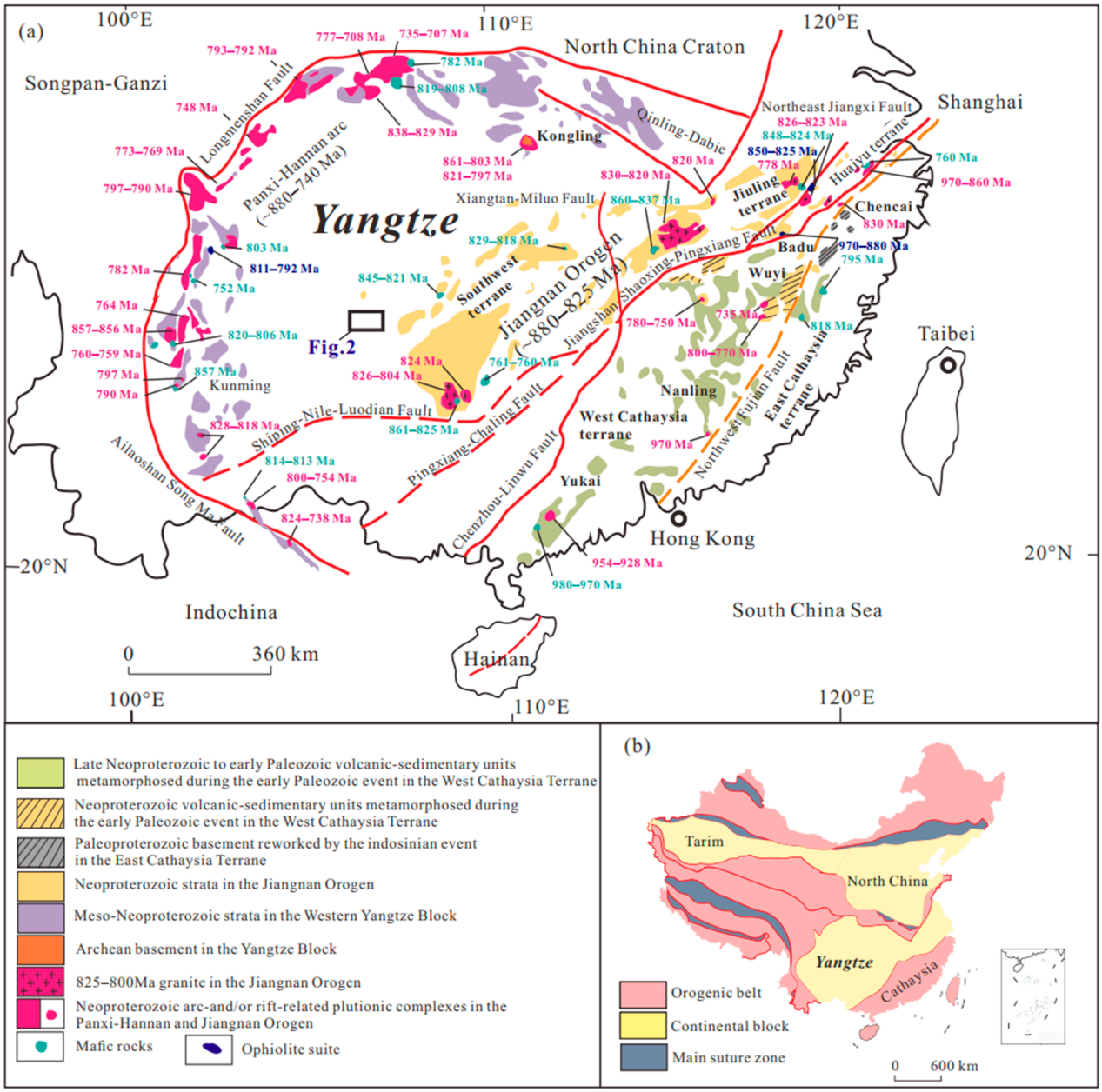

Figure 1. (**a**) Simplified geological map of South China Craton and the distribution of Proterozoic–Paleozoic thermal events. (**b**) Simplified map of the tectonic plate divisions of China. Both (**a**,**b**) are modified after being obtained from [5]. Reprinted from Precambrian Research, 2020, 337, Wang, L.J.; Zhang, K.X.; Lin, S.F.; He, W.H.; Kou, X.H.; and Xiao, H.Z. Turbidite record of a Neoproterozoic active continental margin in the West Cathaysia terrane, South China: implications for the relationships between the Yangtze and Cathaysia blocks and their positions in Rodinia, no. 105457, Copyright (2024), with permission from Elsevier.

During 880–830 Ma, the Yangtze and Cathaysia Blocks were consolidated along the Jiangnan orogenic belt to form the South China Craton [6,7]. Subsequent geological events, such as the Chengjiang Movement (~780–750 Ma), triggered continuous subduction and collision around the Yangtze Block. After the termination of the "Snowball Earth" event around 635 Ma, including the Sturtian and Marinoan glaciations, significant climatic and environmental changes led to a rise in sea level, resulting in the formation of several phosphate deposits [8,9]. Shi [10] suggested that the formation of the Doushantuo Formation in the Sinian of South China is related to the late Neoproterozoic breakup of the Rodinia supercontinent, which provided hydrothermal and mantle-derived mineralizing substances for the formation of the strata. However, there is no consensus on the exact formation age of the Doushantuo Formation. Previous studies using various dating methods on different rock types within the South China Doushantuo Formation suggest an overall formation timeframe between 635–551 Ma [11–15], with limited information on the post-mineralization tectonothermal events in the region.

Located in central Guizhou Province, the Kaiyang phosphate mining area is situated in the central–southern part of the Yangtze Block. This area holds preserved rocks ranging from the Archean to Neoproterozoic ages, thus reflecting the aggregation and breakup of the landmass. Consequently, it serves as an exceptional location for investigating the Yangtze Block, Rodinia, and phosphate deposits. Zircon, a common accessory mineral in crustal rocks, is prevalent in the Doushantuo Formation of Kaiyang. Zircon's U-Pb system possesses a high closure temperature, reaching up to 900 °C, while its fission-track annealing temperatures range from 180 °C to 260 °C [16,17].

These properties enable zircon to document the various stages of magmatic, hydrothermal, and tectonic thermal events it has experienced. The U-Pb ages of younger detrital zircons within stratigraphic layers can establish the minimum age limit for the sedimentary period. Additionally, due to their lower closure temperature, the fission-track system of these zircons can provide insights into the stratigraphy's tectonic uplift, faulting, and hydrothermal activity history.

This study, based on detailed field geological surveys, systematically investigates the lithology, whole-rock geochemistry, LA-ICP-MS zircon U-Pb isotopic geochronology, and low-temperature thermochronology of zircon fission tracks in the phosphorite-bearing rocks, including phosphorite, dolostone, and sandstone, of the Doushantuo Formation in the area. This study aims to reconstruct the pre-mineralization provenance magmatic events, the geological era of mineralization, and the post-mineralization tectonic thermal event history of the Kaiyang phosphate deposit.

2. Regional Geological Background

The Kaiyang phosphate deposit is a significant, large-scale phosphate mine in China, and it is situated approximately 150 km from Guiyang City in the central–southern part of the Yangtze Block. The stratigraphic and lithologic sequence exposed in the Kaiyang area, from oldest to newest, includes the Nanhua Formation of the lower Sinian System, which is characterized by glacial conglomerate; the Doushantuo Formation of the lower Sinian System, which contains phosphorite-bearing rocks; and the Dengying Formation of the upper Sinian System, which is primarily composed of dolomite. Furthermore, the research area lacks Upper Ordovician to Carboniferous strata (Figure 2).

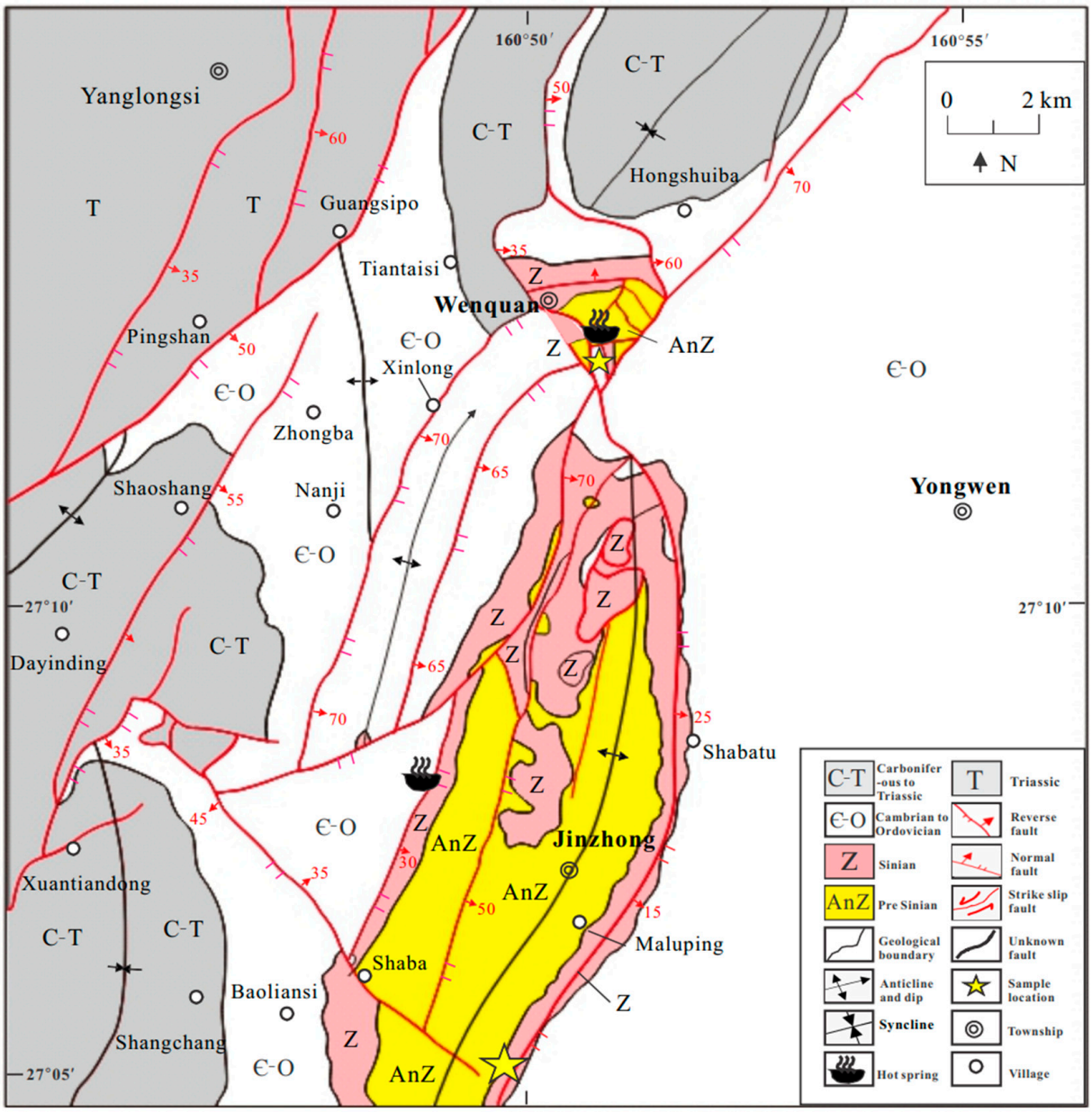

Figure 2. Simplified geological map of the Yangshui anticline area in the Kaiyang area (modified after [18]).

The Doushantuo Formation is the primary layer containing phosphorite deposits in the area, with a thickness ranging from 8.66–40.44 m. This formation is exposed on both limbs of the Yangshui anticline. The phosphate deposits are mainly found underground with few surface outcrops. The orientation and dip of the mining layers align with the stratigraphy, exhibiting stable yield along their strike and dip directions. The average grade of P_2O_5 ranges from 17.65%–35.09% [19]. The lithology of the phosphorite-bearing rocks, from top to bottom, includes the following: a top layer of gray, thinly layered fine-crystalline dolostone; dark gray dolomitic siliceous rock, with the basal layer being siliceous dolostone; dark gray laminated phosphorite, where fine-grained pyrite is visible in impregnation form; light-gray-to-dark-gray-banded dolomitic phosphorite; and a basal layer of greenish-gray thick sandstone (Figures 3 and 4).

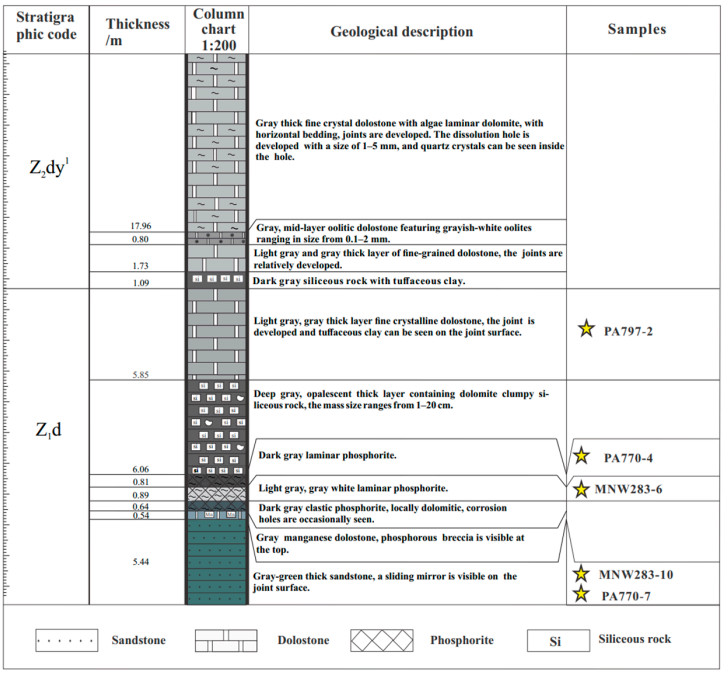

Figure 3. Stratigraphic column diagram illustrating the phosphorite-bearing rocks in the Kaiyang area of Guizhou, from the Doushantuo Formation to the overlying Dengying Formation. The yellow asterisks denote the following sampled intervals: PA797-2 for top dolostone, PA770-4 and MNW283-6 for phosphorite rock, and MNW283-10 and PA770-7 for basal sandstone.

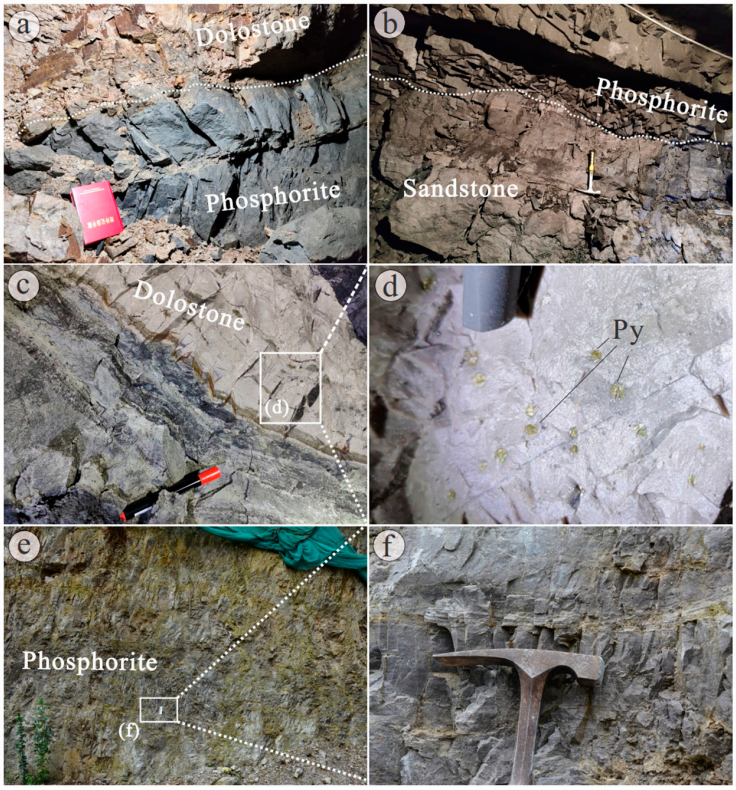

Figure 4. Underground (**a**–**d**) and surface outcrop (**e**,**f**) photos of the phosphorite-bearing rocks of the Doushantuo Formation in the Kaiyang area. (**a**) Top dolostone overlying phosphorite; (**b**) phosphorite overlying basal sandstone; (**c**) pyrite-containing top dolostone; (**d**) pyrite in dolostone; (**e**) weathered surface showing greenish-gray, banded phosphorite; and (**f**) fresh surface showing grayish-white, banded phosphorite.

The Kaiyang phosphate mining area is characterized by well-developed folds and fractures, with the main structural trends oriented primarily in the northwest–southeast, nearly north–south, directions. The Yangshui anticline, a key controlling structure for the phosphate mine, extends in a north–northeast (NNE) direction. It spans a total length of 26 km, with a width varying between 4 and 5 km. The anticline exhibits a dip angle of approximately 30 degrees. The western limb exhibits a stratum dip angle ranging from 15 to 60 degrees, whereas the eastern limb ranges from 19 to 50 degrees. The area covered by the anticline totals 120 square kilometers. Along the limbs of the Yangshui anticline, in the Jinzhong area, evident uplift can be observed. The core exhibits strata with a gentler inclination. Several faults intersect the axis and limbs, resulting in the exposure of phosphorite-bearing strata at the surface north of Jinzhong area due to tectonic uplift and faulting. This activity results in the repetition and displacement of the phosphorite-bearing strata [10].

3. Petrography

The phosphorite-bearing rocks in the Kaiyang area represent a unique phosphate stratum sequence, where the phosphate-bearing layers may form under various geological environments in different regions, thus leading to distinct mineral compositions. In Kaiyang, phosphorite is a predominant phosphate ore within the phosphorite-bearing rocks, which are typically grayish-white, light gray, or dark gray. It primarily features clastic or granular structures. The phosphorite and its surrounding rocks frequently form banded or massive structures (Figure 5a–c).

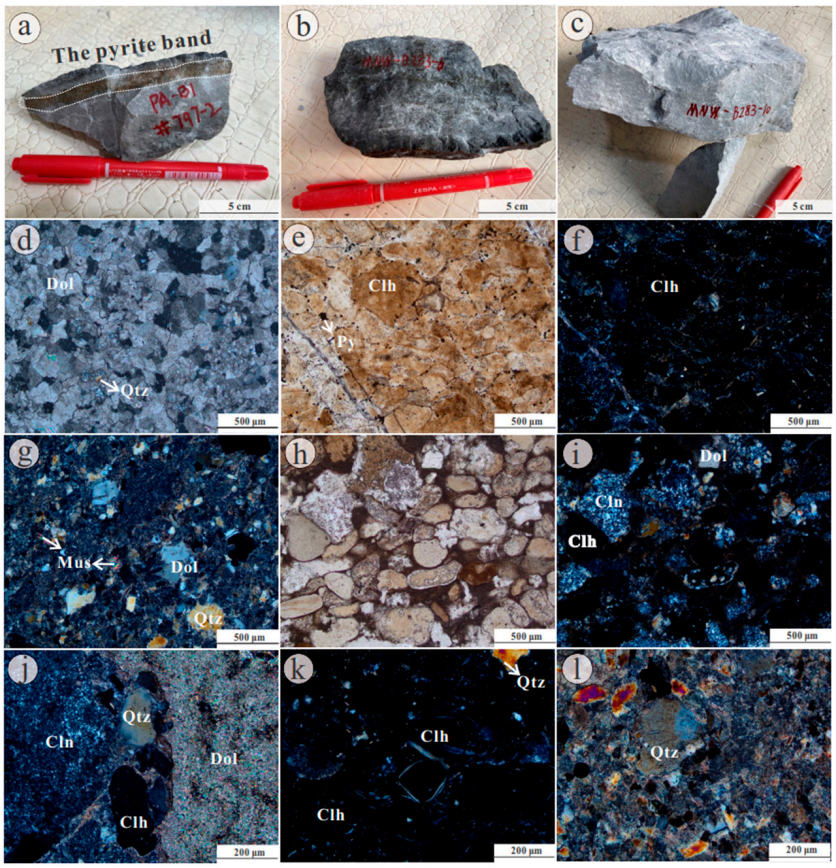

Figure 5. Specimen photographs (**a**–**c**) and petrographic photomicrographs (**d**–**l**) of phosphorite-bearing rocks. (**a**,**d**,**j**) Pyrite-banded dolomitic phosphorite; (**b**,**e**,**f**,**k**) striped phosphorite; (**h**,**i**) siliceous phosphorite; and (**c**,**g**,**l**) basal sandstone. Abbreviations: Py = pyrite; Dol = dolomite; Qtz = quartz; Clh = collophane; Mus = muscovite; and Cln = chalcedony. The mineral names and abbreviations are referenced from [20].

The top layer rock of the phosphorite-bearing rocks was found to be dolostone, mainly consisting of dolomite (>50%), with quartz and collophane grains occasionally being interspersed between it (about 5%–10%) (Figure 5d). The primary mineral in the phosphorite was found to be collophane (about 10%–70%) (Figure 5e,f). However, there were also clay minerals (about 5%–10%) found that were infrequently distributed among the clasts, whereby they usually occurred as matrix components (Figure 5g). Lastly, dolomite and quartz were found to be the more abundant minerals (about 10%–30%) in this region closely associated with the collophane (Figure 5h–j). The collophane grain sizes were around 0.01–1.00 mm, with some collophane granules displaying zonal structures (Figure 5k). The basal layer of the phosphorite-bearing rocks was sandstone, primarily consisting of quartz (about 40%), collophane (about 10%), and dolomite (about 5%–20%) (Figure 5l).

While the mineral compositions varied across the different layers of the phosphorite-bearing rocks, siliceous minerals and pyrite were found to be the prominent accessory minerals. Notably, quartz and chalcedony were found to share a close symbiotic relationship with the collophane (Figure 5h–j), either filling within the collophane as authigenic chalcedony (Figure 5i) or were interspersed as detrital quartz (Figure 5g,j). The pyrite frequently occurred in a stellate (Figure 4d) or banded pattern (Figure 5a) within the phosphorite-bearing rocks, exhibiting widespread distribution.

4. Analytical Methods

4.1. Whole-Rock Geochemical Analysis

Five representative fresh rock samples were selected for a comprehensive analysis of major and trace elements. Sample PA797-2 is a dolostone from the top of the ore body, samples MNW283-6 and PA770-4 are phosphorite from the ore body, and samples MNW283-10 and PA770-7 are sandstone from the bottom of the ore body.

An analysis of the major and trace elements was conducted at Ausreal Testing & Analysis Co., Ltd., Guangzhou, China. Major elements were analyzed using the fused bead method, employing an X-ray fluorescence spectrometer (XRF) with a precision of 10^{-2}. The specific procedure was as follows: Fresh rock samples were crushed, and 300 g was subsampled and ground to 75 μm (200 mesh). The ground sample was placed in a platinum crucible and mixed with a lithium borate–lithium metaborate–lithium nitrate flux ($LiBO_2/Li_2B_4O_7$). After a thorough mixing of the sample and flux, they were melted in a high-precision fusion machine at 1050 °C. The melted product was poured into a platinum mold to cool and form a flat-fused bead, which was then checked for quality. The bead was dissolved in nitric acid, hydrochloric acid, and hydrofluoric acid; then, it was brought to volume, and the major element content was determined using XRF.

For the trace element analysis, the dried sample was weighed and placed in a high-pressure, sealed Teflon container, to which 2 mL of HF, 0.6 mL of HNO_3, and 1 mL of $HClO_4$ were added sequentially. The container was then heated at a constant temperature of 185 °C for 72 h, after which it was cooled to 105 °C to dry the sample to a wet salt state. An additional 2 mL of HNO_3 was added to the container to redissolve the sample, and after maintaining at 105 °C for another 12 h, the trace elements were determined using an Inductively Coupled Plasma Mass Spectrometer (Agilent ICP MS 7500).

4.2. Zircon LA-ICP-MS U-Pb Dating

In this study, four representative fresh rock samples were selected for LA-ICP-MS zircon U-Pb dating: phosphorite MNW283-6, sandstones MNW283-10 and PA770-7, and dolostone PA797-2. The preparation of zircon single mineral targets, the acquisition of cathodoluminescence (CL) images, U-Pb isotope dating, and rare earth element (REE) analysis were all carried out at Sample Technology Co., Ltd., Wuhan, China. The specific procedures are detailed below.

The rock samples were crushed, washed, and separated by heavy liquid and electromagnetic techniques. Under a binocular microscope, zircon grains with intact crystal forms and representative characteristics were selected and mounted on a resin platform, which

were then ground and polished to create targets. Comprehensive analyses using reflected light, transmitted light microscopy, and CL imaging were performed on the zircon targets. Based on these analyses, the areas that were far from the grain edges and without cracks or inclusions were selected as optimal spots for subsequent testing.

The LA-ICP-MS analysis system's GeolasPro laser ablation system was composed of a COMPexPro 102 ArF 193 nm excimer laser and a MicroLas optical system, with the ablation system connected to the Agilent 7900 mass-spectrometer. High-purity helium was used as the carrier gas for the ablated material, with a laser spot size of 32 μm. Each time-resolved analysis consisted of approximately 20–30 s of blank signal and 50 s of sample signal, with a pulse frequency of 5 Hz and a laser energy of 80 mJ. The instrument was tuned to optimal conditions using the NIST 610 reference material before testing, thus ensuring that the signals for ^{139}La and ^{232}Th were maximized and the oxide production rate ^{232}Th^{16}O/^{232}Th was less than 0.3%. The experimental results were calibrated using the zircon standard GJ-1 as an external standard, and ^{29}Si was used as an internal standard for correcting U-Pb isotope fractionation effects and mass bias.

The final isotopic and trace element results were corrected using Iolite 4 software, and the ratios, errors, and correlation coefficients necessary for Wetherill concordia diagrams were obtained. The zircon U-Pb age results were calculated using the Isoplot R online website [21], thereby producing Wetherill concordia diagrams and age frequency distributions.

4.3. Zircon Fission-Track Analysis

In this study, four representative fresh rock samples (sandstone MNW283-10, phosphorite PA770-4, sandstone PA770-7, and dolostone PA797-2) were selected for zircon fission-track (ZFT) analysis, and the analyses were conducted at Zekangen Technology Co., Ltd., Beijing, China. The experimental procedure was as follows: Selected single zircon grains were evenly placed on a slide and covered horizontally with a Teflon piece measuring 1.6 cm × 1.6 cm. The setup was then uniformly heated on a hot plate and slowly pressed vertically until the zircon grains were embedded in the Teflon. After cooling, the slide was removed and the zircon grains were polished with sandpaper until the internal surfaces of the minerals were exposed. The samples were etched with a 1:1 NaOH/KOH eutectic mixture for 25 h at temperatures between 210–230 °C to reveal spontaneous tracks. Mica sheets were placed over the samples and fixed with tape for triangular punching. The samples, reference material (FCT), and standard glass (CN5) were irradiated sequentially in a nuclear reactor, with the neutron flux calibrated using the CN5 standard glass and set at 1.2×10^{15} cm^{-2}·s^{-1}. After separating the mica from the samples, the mica was etched in a 40% HF solution for 20 min to reveal the induced tracks, and it was then washed and checked to ensure that there was no deformation of the sample target before measuring the spontaneous and induced track densities using the AUTOSCAN system. The central age and error of the fission tracks were calculated using the Zeta calibration method recommended by IUGS [22]. The chi-square test value P(χ^2) is a crucial parameter for assessing whether the measured single grain ages belong to a uniform age group. When P(χ^2) > 5%, the fission-track ages are uniformly distributed and belong to the same age group, thus allowing for the calculation of a pooled age. If P(χ^2) < 5%, it suggests the presence of multiple age groups and indicates a complex genesis that does not conform to a normal distribution, thus necessitating a binomial fit analysis to decompose the fission-track ages into multiple peak ages. The youngest peak age generally represents the most recent thermal event recorded by the grain components that have undergone low-temperature annealing [23,24].

5. Analytical Results

The whole-rock geochemistry results are presented in Tables 1 and 2, and the results of the zircon fission-track analysis are presented in Table 3. The zircon LA-ICP-MS U-Pb dating isotopes and trace element data are presented in Supplementary Tables S1 and S2. The single grain zircon fission-track ages and related parameters can be found in Supplementary

Table S3. In the analysis of zircon age spectra and the accompanying text, $^{206}Pb/^{238}U$ ages were selected for zircons younger than 1000 Ma, while $^{207}Pb/^{206}Pb$ ages were used for zircons older than 1000 Ma.

Table 1. The major element oxide content in the samples (wt. %, on a whole-sample basis).

Samples	Rock Type	Al_2O_3	BaO	CaO	TFe_2O_3	K_2O	MgO	MnO	Na_2O	P_2O_5	SiO_2	SO_3	SrO	TiO_2	LOI
MNW283-6	Phosphorite	2.96	0.17	41.70	1.78	0.21	1.15	0.04	0.04	30.10	18.44	3.63	0.09	0.04	2.96
PA770-4	Phosphorite	1.93	0.18	48.10	0.60	0.19	0.18	0.04	0.24	34.80	10.14	1.43	0.08	0.04	1.93
MNW283-10	Sandstone	3.50	0.02	20.00	1.03	1.07	14.30	0.45	0.03	0.05	26.56	0.97	0.01	0.23	31.41
PA770-7	Sandstone	10.08	0.03	2.14	2.10	3.10	1.92	0.04	0.02	0.30	74.42	2.68	0.01	0.50	4.71
PA797-2	Dolostone	0.78	0.02	21.90	12.58	0.25	13.70	0.24	0.07	2.08	12.10	23.60	0.02	0.04	15.85

Table 2. Trace element concentrations and rare earth element contents of the studied samples (ppm, on a whole-sample basis).

Samples Rock Type	MNW283-6 Phosphorite	PA770-4 Phosphorite	MNW283-10 Sandstone	PA770-7 Sandstone	PA797-2 Dolostone
Li	2.10	12.10	11.00	24.90	3.10
Be	0.32	1.61	0.59	1.27	0.38
Sc	0.90	1.50	2.60	5.90	1.00
V	16.00	5.00	51.00	36.00	8.00
Cr	9.00	9.00	11.00	25.00	5.00
Co	29.60	3.00	8.60	18.80	4.30
Ni	10.30	2.60	5.20	11.90	3.60
Cu	564.00	22.70	7.30	119.00	20.60
Zn	54.00	4.00	15.00	15.00	81.00
Ga	1.40	1.00	5.30	11.90	0.90
Rb	5.10	5.10	27.50	77.20	5.40
Sr	758.00	690.00	119.00	56.10	81.20
Mo	3.47	0.96	1.35	0.55	1.66
Cd	0.11	0.02	0.31	0.02	0.52
In	0.048	0.005	0.066	0.037	0.083
Sb	17.30	0.73	0.45	0.69	1.48
Cs	1.18	0.50	3.71	10.85	0.73
Ba	1445.00	1465.00	160.50	224.00	110.00
W	1.50	0.50	1.40	1.70	0.20
Tl	1.50	0.10	0.27	0.48	0.20
Pb	29.50	6.40	7.00	8.00	290.00
U	14.35	15.30	1.82	2.07	2.38
Nb	1.50	1.40	6.10	13.60	0.90
Ta	0.05	0.05	0.37	0.86	0.05
Zr	43.00	25.00	192.00	266.00	39.00
Hf	0.70	0.30	4.50	6.50	0.80
La	14.10	35.40	16.00	27.80	5.00
Ce	37.10	91.20	34.40	50.40	9.80
Pr	4.78	11.95	3.54	4.58	1.41
Nd	25.00	57.70	13.20	15.00	5.80
Sm	8.05	14.60	2.48	2.58	1.20
Eu	2.05	4.14	0.46	0.54	0.30
Gd	9.57	17.20	1.99	2.83	1.27
Tb	1.09	2.33	0.30	0.57	0.20
Dy	6.23	13.55	1.94	3.91	1.14
Ho	1.38	2.96	0.42	0.89	0.25
Er	3.91	8.18	1.35	2.87	0.67
Tm	0.51	1.01	0.22	0.46	0.10
Yb	2.86	5.54	1.53	3.12	0.54
Lu	0.38	0.79	11.70	23.60	8.40
Y	53.40	109.50	1.53	3.12	0.54

Table 3. Fission-track analytical results of the samples from the Kaiyang phosphorite-bearing rocks.

Samples	Rock Type	n	ρ_s (10^5/cm^2)	N_S	ρ_i (10^5/cm^2)	N_i	N_d	P(χ^2) (%)	Central Age (±1σ) (Ma)	Pool Age (±1σ) (Ma)
MNW283-10	Sandstone	26	235.82	3454	14.01	410	7661	78.80	501 ± 31	501 ± 31
PA770-7	Sandstone	40	204.98	4695	13.10	720	7661	51.20	366 ± 20	366 ± 19
PA797-2	Dolostone	34	151.90	6152	14.93	802	7661	5.80	489 ± 28	489 ± 25
PA770-4	Phosphorite	26	84.91	1636	12.43	1685	7661	0	53 ± 5	53 ± 3

Note: n = number of dated zircon crystals; ρ_s (ρ_i) = spontaneous (induced) track densities ($\times 10^5$ tracks/cm^2); N_s (N_i) = number of counted spontaneous (induced) tracks; N_d = number of tracks counted on dosimeter; and P(χ^2) = probability obtaining chi-square value for n degrees of freedom. Zeta value of 88.2 ± 2.9.

5.1. Whole-Rock Geochemical Analysis

The phosphorite-bearing rocks examined in this study were characterized by abundant P_2O_5, CaO, SiO_2, and MgO, exhibiting significant variations in chemical composition across different lithologies (Table 1). The top dolostone sample (PA797-2) alone had MgO and SiO_2 contents of 13.70% and 12.10%, respectively, with relatively high TFe_2O_3 (12.58%) and SO_3 (23.60%) contents (which was attributed to the abundance of pyrite within the sample). The phosphorite samples (MNW283-6 and PA770-4) contained 30.10% to 34.80% P_2O_5, 41.70% to 48.10% CaO, and 10.14% to 18.44% SiO_2, alongside elevated Al_2O_3 levels (1.93% to 2.96%). In contrast, the basal sandstone samples (MNW283-10 and PA770-7) showed a wide range of SiO_2 content from 26.56% to 74.42%, variable MgO content from 1.92% to 14.30%, and notably higher Al_2O_3 levels that ranged from 3.50% to 10.08% (with an average of 6.79%).

The phosphorite samples (MNW283-6 and PA770-4) showed higher concentration of P and Y but were characterized by relatively lower concentrations of Hf and Zr compared to the other samples. The sandstone samples (MNW283-10 and PA770-7) showed higher concentrations of Rb, Th, K, Nb, Zr, and Hf. In contrast to both the sandstone and phosphorite samples, the dolostone sample (PA797-2) generally did not show an enrichment of trace elements (Figure 6a).

The phosphorite-bearing rocks exhibited an enrichment in middle REEs and a depletion in light and heavy REEs (Figure 6b). The total REE content in these rocks varied significantly across different lithologies: the dolostone sample contained 27.76 ppm; the phosphorite samples ranged from 117.01 to 266.55 ppm, averaging 191.78 ppm; and the sandstone samples ranged from 78.07 to 116.04 ppm, with an average of 97.06 ppm. A notable positive correlation was found to exist between the P_2O_5 content and total REE concentration (R^2 = 0.44) (Figure 6c). An even stronger positive correlation was observed between the P_2O_5 content and Y concentration (R^2 = 0.77) (Figure 6d); conversely, there was a significant negative correlation with the La_N/Yb_N ratio (R^2 = 0.79) (Figure 6e).

The dolostone sample PA797-2 exhibited a minor negative Ce anomaly, as indicated by a δCe value of 0.85 (where $\delta Ce = Ce_N/Ce_N^*$, $Ce_N^* = \sqrt{La_N * Pr_N}$). Conversely, it displayed a weak positive Eu anomaly with a δEu value of 1.14 (where $\delta Eu = Eu_N/Eu_N^*$, $Eu_N^* = \sqrt{Sm_N * Gd_N}$). The La_N/Yb_N ratio for this sample was 0.68, and the Y_N/Ho_N ratio was 1.23. The REE distribution patterns of the two phosphorite samples were broadly similar, with δCe values ranging from 1.02 to 1.04, thus showing no clear Ce anomaly. Their δEu values ranged from 1.10 to 1.23, indicating weak positive anomalies. The La_N/Yb_N ratios for these samples varied between 0.36 and 0.47, while the Y_N/Ho_N ratios were between 1.36 and 1.42. Two of the sandstone samples showed similar distribution curves, with their δCe values ranging from 1.03 to 1.05, thus suggesting no significant Ce anomaly. Their δEu values varied between 0.94 and 0.98, indicating weak negative anomalies. The La_N/Yb_N ratios for these samples were between 0.66 and 0.77, and the Y_N/Ho_N ratios were between 0.97 and 1.02.

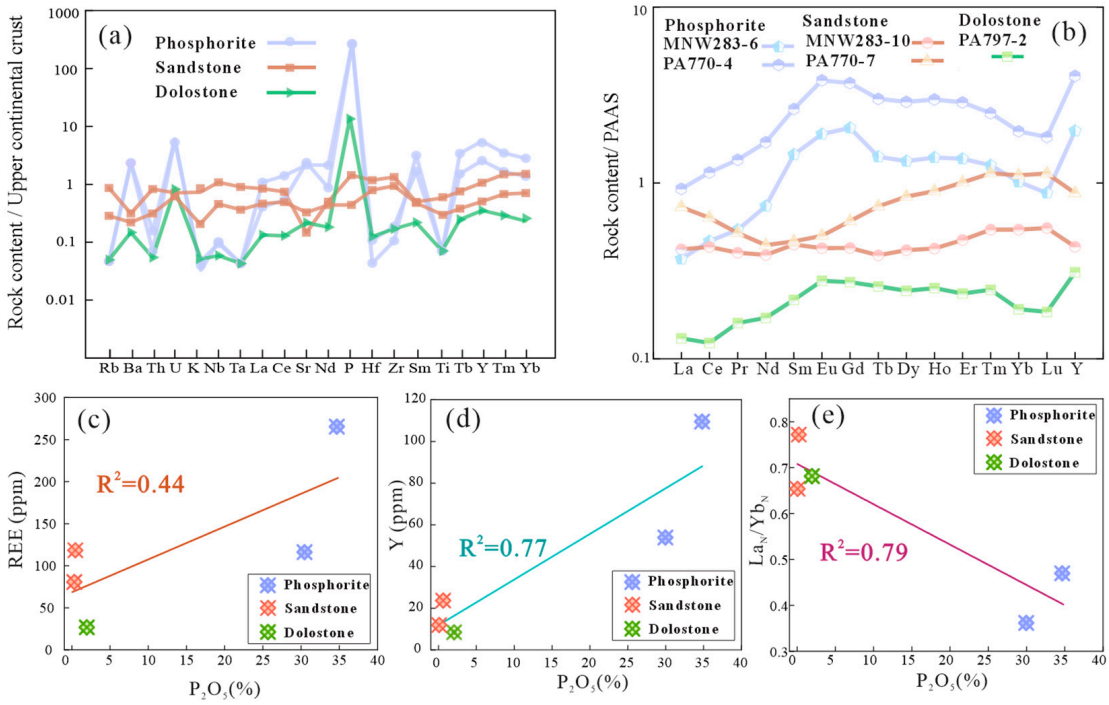

Figure 6. Diagrams illustrating the whole-rock geochemical compositions for the Kaiyang phosphorite-bearing rocks. (**a**) A trace element spider diagram normalized to the upper continental crust values (data referenced from [25]); (**b**) rare earth element normalized distribution pattern diagram (PAAS-normalized data from [26]); (**c**) correlation chart of the P_2O_5 and total REE content; (**d**) correlation chart of the P_2O_5 and Y content; and (**e**) correlation chart of the P_2O_5 content and La_N/Yb_N ratio.

5.2. Zircon LA-ICP-MS U-Pb Dating

In our study, the zircon grains ranged from 35 to 150 μm in length and 30 to 60 μm in width, with aspect ratios ranging from 1:1 to 2:1. Over 70% of the zircon grains were small, highly rounded, had blurred edges, and had some apparent fragmentation (e.g., Figure 7d, nos. 32 and 33). The CL images show that most of the selected zircon grains had distinct rhythmic zoning (e.g., Figure 7a, no. 39), while a few exhibited weak zoning or uniform internal structures (e.g., Figure 7c, no. 23 and 38). Due to the small size of the zircon grains in the phosphorite-bearing rocks, combined with their complex internal structures and high inclusion content, the number of micro-areas suitable for analysis was limited. In this study, we obtained a total of 155 valid data points from four samples that encompassed three distinct lithologies.

In the phosphorite sample MNW283-6, our analysis of 41 zircon grains yielded 35 valid data points. The ages of these grains spanned from 2508 to 594 Ma, with prominent age peaks at around 780 Ma, 820 Ma, and 880 Ma. The weighted mean $^{206}Pb/^{238}U$ ages of the three peak groups were 877 ± 3 Ma (N = 13, MSWD = 3.30); 825 ± 4 Ma (N = 8, MSWD = 0.59); and 777 ± 4 Ma (N = 8, MSWD = 0.19) (Figure 8a,b). The oldest and youngest zircons in the aforementioned sample registered at $^{207}Pb/^{206}Pb$ ages of 2508 ± 28 Ma and 1837 ± 29 Ma, and $^{206}Pb/^{238}U$ ages of 651 ± 29 Ma and 594 ± 9 Ma, respectively. The Th/U ratios ranged from 0.33 to 1.57 (Figure 8d).

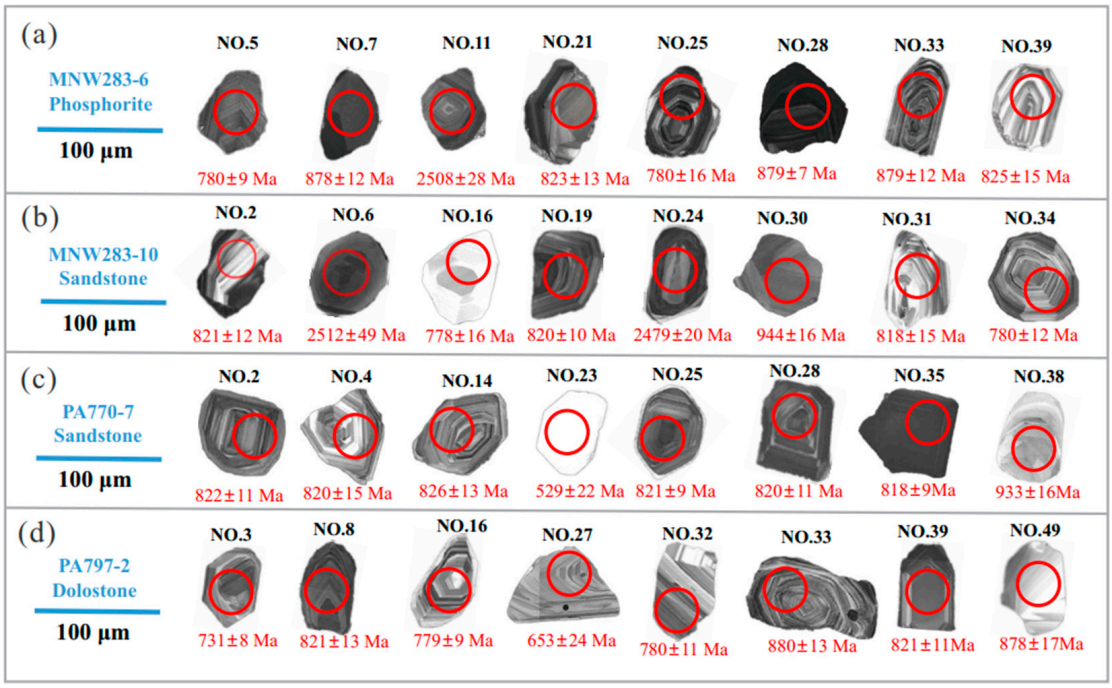

Figure 7. (**a**–**d**) Representative CL images of the zircon grains from the Kaiyang phosphorite-bearing rocks (red circles indicate analysis locations).

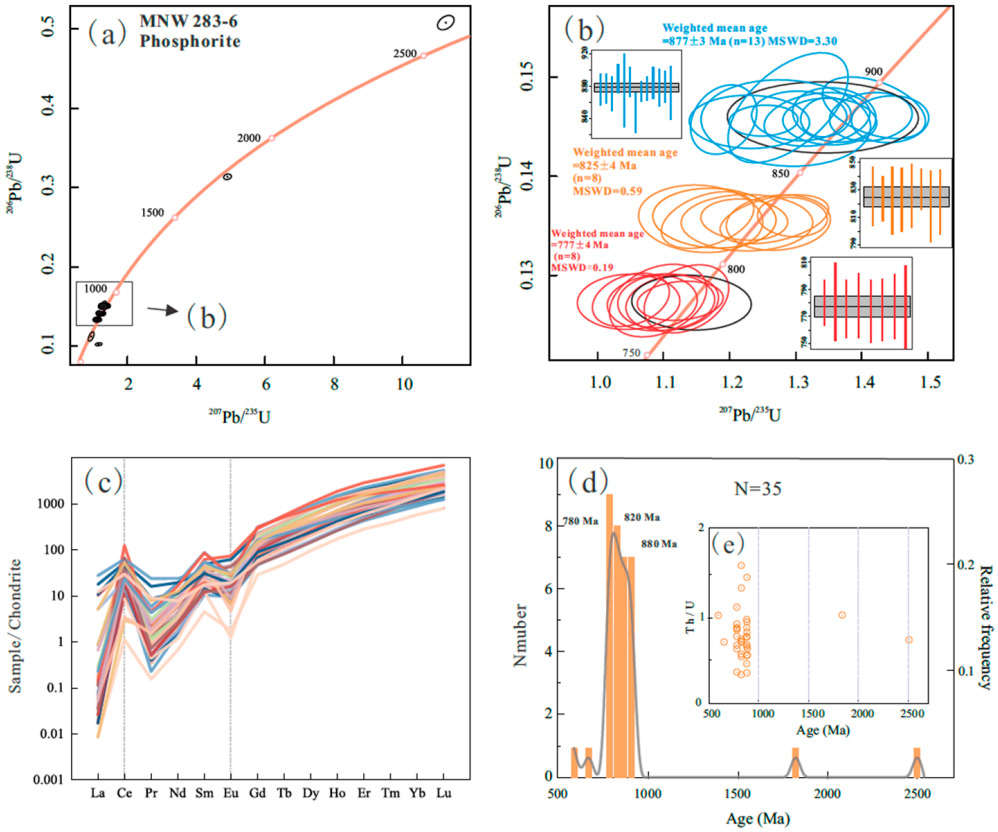

Figure 8. Phosphorite sample MNW283-6 zircon U-Pb age-analysis-related diagrams. (**a**,**b**) Concordia diagrams; (**c**) chondrite-normalized REE distribution pattern diagram (C1 chondrite normalization data from [27]); (**d**) U-Pb age histograms and the relative probability plots; and (**e**) correlation diagrams of the zircon ages and Th/U ratio diagram. The $^{206}Pb/^{238}U$ ages were selected for zircons younger than 1000 Ma, while $^{207}Pb/^{206}Pb$ ages were used for zircons older than 1000 Ma.

In the basal sandstone sample MNW283-10, we retained 36 valid data points, with ages ranging from 2512 Ma to 777 Ma and two marked peaks around 820 Ma and 780 Ma. The weighted mean $^{206}Pb/^{238}U$ ages of the two peak groups were 819 ± 2 Ma (N = 19, MSWD = 0.30) and 779 ± 4 Ma (N = 7, MSWD = 1.40) (Figure 9a,b). Additionally, two zircon grains recorded ages of 2512 ± 49 Ma and 2479 ± 20 Ma. The Th/U ratios for all measured zircons ranged from 0.39 to 1.47 (Figure 9d).

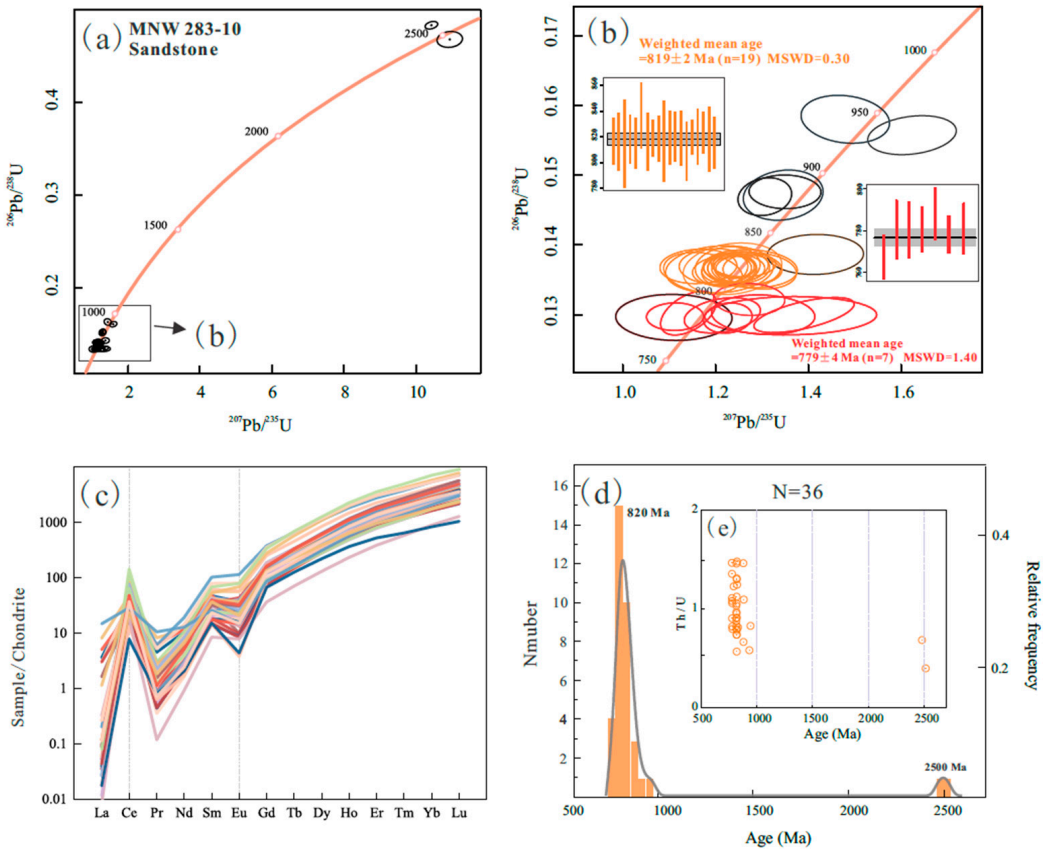

Figure 9. Sandstone sample MNW283-10 zircon U-Pb age analysis-related diagrams. (**a**,**b**) Zircon concordia diagrams; (**c**) zircon chondrite-normalized REE distribution pattern diagram (C1 chondrite normalization data from [27]); (**d**) U-Pb age histograms and the relative probability plots; and (**e**) correlation diagrams of the zircon ages and Th/U ratio diagram. $^{206}Pb/^{238}U$ ages were selected for zircons younger than 1000 Ma, while $^{207}Pb/^{206}Pb$ ages were used for zircons older than 1000 Ma.

For basal sandstone sample PA770-7, 38 data points were considered valid, with ages ranging from 2032 Ma to 529 Ma. The weighted mean $^{206}Pb/^{238}U$ age of the peak group is 819 ± 2 Ma (N = 25, MSWD = 0.50) (Figure 10a,b). The two youngest zircons in this sample were aged at 529 ± 22 Ma and 657 ± 9 Ma, while the three oldest zircon grains recorded ages of 1941 ± 46 Ma, 2016 ± 48 Ma, and 2032 ± 41 Ma. The Th/U ratios for all measured zircons are between 0.28 and 2.82 (Figure 10d).

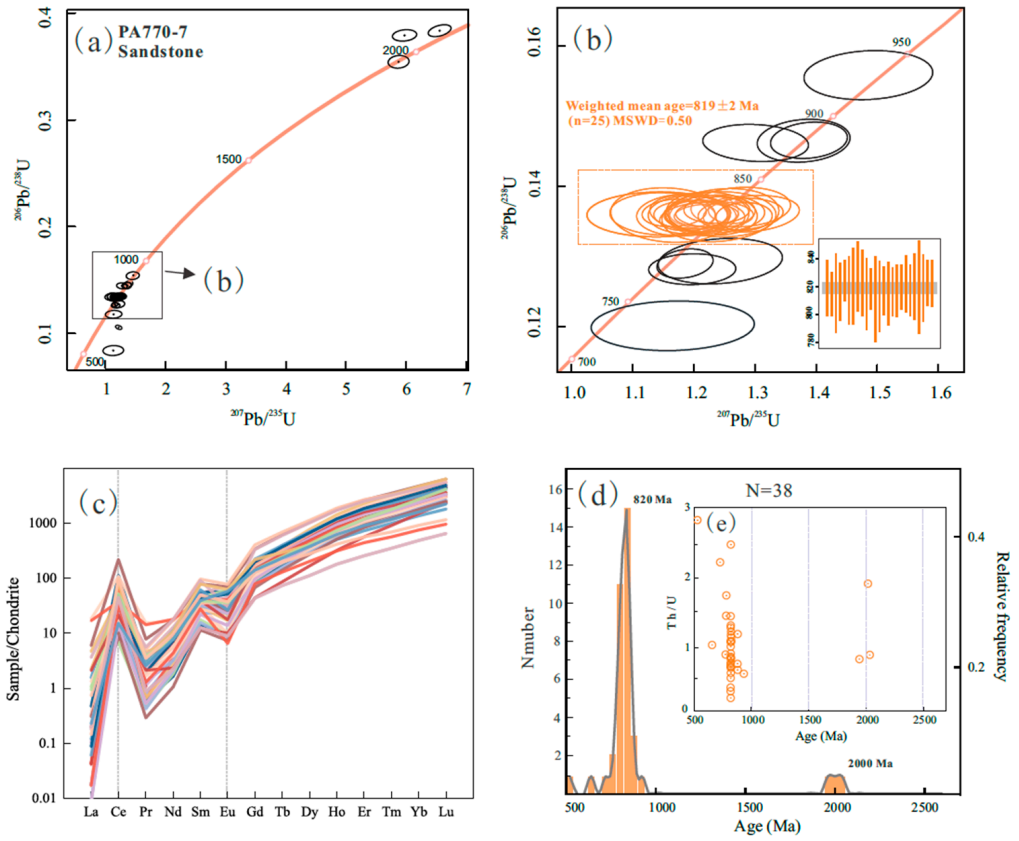

Figure 10. Sandstone sample PA770-7 zircon U-Pb age analysis-related diagrams. (**a**,**b**) Zircon concordia diagrams; (**c**) zircon chondrite-normalized REE distribution pattern diagram (C1 chondrite normalization data from [27]); (**d**) U-Pb age histograms and the relative probability plots; and (**e**) correlation diagrams of the zircon ages and Th/U ratio diagram. $^{206}Pb/^{238}U$ ages were selected for zircons younger than 1000 Ma, while $^{207}Pb/^{206}Pb$ ages were used for zircons older than 1000 Ma.

An analysis of 49 zircon grains from the top dolostone sample PA797-2 yielded 46 valid data points. The ages of these zircons ranged from 2318 Ma to 653 Ma, with a primary peak at approximately 820 Ma and secondary peaks at around 780 Ma and 880 Ma. The weighted mean $^{206}Pb/^{238}U$ ages of the three peak groups were 878 ± 4 Ma (N = 8, MSWD = 1.00), 818 ± 2 Ma (N = 27, MSWD = 0.86), and 780 ± 4 Ma (N = 6, MSWD = 0.13) (Figure 11a,b). The oldest and youngest zircons in that sample recorded ages of 2318 ± 47 Ma and 653 ± 24 Ma, respectively. The Th/U ratios for all zircons spanned from 0.30 to 1.97 (Figure 11d).

Using the zircon Ti-in-zircon thermometry method formulated by Watson et al. [28], we calculated the crystallization temperatures of the zircons through the application of the T(K) = 5080 ± 30/(6.01 ± 0.03) − log (Ti) equation. The Ti content within the zircons from our samples ranged from 1.81 ppm to 584.03 ppm, thus yielding an average crystallization temperature for the zircons of 733 °C. A comprehensive assessment of 155 valid zircon data points revealed a distinctive REE distribution pattern characteristic of the magmatic zircons, which exhibited an enrichment of heavy REEs (HREEs) across the spectra, with notable positive Ce anomalies and subtle negative Eu anomalies. This trend indicated a relative depletion in light REEs, which was a contrast to the enrichment in medium-to-heavy REEs (Figures 8c, 9c, 10c and 11c), thus offering valuable perspectives on the magmatic processes and the geochemical conditions under which the zircons formed.

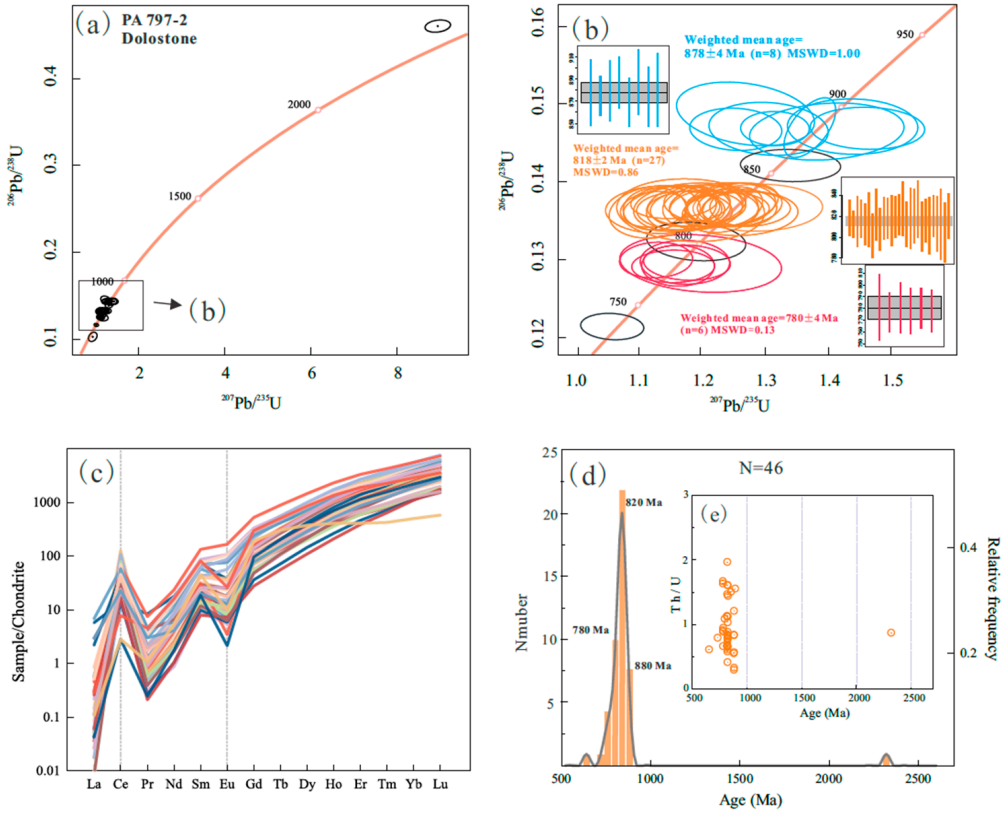

Figure 11. Dolostone sample PA797-2 zircon U-Pb age analysis-related diagrams. (**a**,**b**) Zircon concordia diagrams; (**c**) zircon chondrite-normalized REE distribution pattern diagram (C1 chondrite normalization data from [27]); (**d**) U-Pb age histograms and the relative probability plots; and (**e**) correlation diagrams of the zircon ages and Th/U ratio diagram. $^{206}Pb/^{238}U$ ages were selected for zircons younger than 1000 Ma, while $^{207}Pb/^{206}Pb$ ages were used for zircons older than 1000 Ma.

5.3. Zircon Fission-Track Analysis

The chi-square test (χ^2) serves as a critical tool in analyzing zircon fission-track (ZFT) sample ages. It helps to adjudicate whether the ages assemble within a singular ensemble or exhibit dispersion, thus aligning them within established guidelines [29]. The 5% threshold serves as the statistical boundary, where exceeding this value indicates a unimodal age distribution within a sample, which is suggestive of a distinct geochronological event. Values below the threshold indicate diverse age distributions, thus necessitating further age decomposition [30]. Our examination employed the ZFT methodology across four different samples, each comprising 26 to 40 grains. Remarkably, the sandstone samples MNW283-10 and PA770-7, along with the dolostone sample PA797-2, exhibited chi-square values ($P\chi^2$) of 78.8%, 51.2%, and 5.8%, respectively, thus transcending the 5% benchmark and signifying age uniformity. In contrast, the phosphorite sample PA770-4, with a $P\chi^2$ of 0%, did not align with this criterion, thus reflecting its age range's diversity due to distinct provenance and geochemical characteristics (Table 3).

For samples meeting the chi-square standard ($P\chi^2 > 5\%$), age pooling yielded a consolidated ZFT age. However, for samples like PA770-4 (phosphorite), which fall below the chi-square threshold, it becomes essential to categorize the grain ages into discrete clusters, apply the central age (central age) for the sample's fission-track age, and utilize the Zeta calibration endorsed by the International Union of Geological Sciences (IUGS) (this investigation adopted a Zeta value of 88.2 ± 2.9 [31]).

Our results indicated pooled ages of 501 ± 31 Ma and 366 ± 19 Ma for the sandstone samples MNW283-10 and PA770-7, respectively, and a pooled age of 489 ± 25 Ma for the dolostone sample PA797-2. For the phosphorite sample PA770-4, the central age was

computed at 53 ± 5 Ma. Age stratification for that sample revealed peaks around 39 Ma and 52 Ma, thus providing refined insights into the thermal history and tectonic progression of the analyzed region.

6. Discussion

6.1. Origin and Age Distribution of Zircon in the Phosphorite-Bearing Rocks of the Doushantuo Formation in the Kaiyang Area

Zircon is highly valued for its robust closure temperature and high melting point, which enables it to document a succession of magmatic events, thus providing invaluable insights into magmatic evolution. The U-Pb age spectrum of detrital zircons emerges as a pivotal tool in delineating the tectonic and magmatic narratives of source terrains, thereby enhancing our understanding of provenance and crustal evolution [32,33].

In the phosphorite-bearing rocks of the Doushantuo Formation in the Kaiyang area, zircons can be primarily categorized into the following types: (1) most zircon grains exhibit a fragmented appearance and a certain degree of rounding, but their CL images show the zoning characteristics of magmatic zircons coupled with high Th/U ratios (>0.2), thus indicating that they are detrital zircons of magmatic origin (e.g., Figure 7a, no. 25, no. 33; Figure 7c, no. 14; Figure 7d, no. 33) [34]; (2) some zircon CL images exhibit characteristics inconsistent with magmatic zoning structures, and their interiors appear relatively homogeneous, indicating a potential metamorphic origin (e.g., Figure 7b, no. 16; Figure 7c, no. 23).

Trace elements like U, Hf, and REEs are crucial in determining the origins of zircon-bearing rocks due to their size and charge, which allows them to fit into zircon's lattice, thus differentiating them from typical silicate minerals [35,36]. Additionally, some of the zircons exhibited a pattern of relative depletion, with a Th/U ratio of 0.30 (Figure 11c), in the medium-to-heavy rare earth elements that were represented on the rare earth element normalized diagram. The CL images revealed clear magmatic zoning without metamorphic rims. The Th/U ratio, combined with the CL images, confirmed their magmatic genesis. The relative depletion in the medium-to-heavy rare earth elements could be attributed to the preferential partition of these elements into the other minerals that co-crystallized with zircon from the parental magma. Further insights obtained from the $(Sm/La)_N - \omega(La)$ and $Ce/Ce^* - (Sm/La)_N$ diagrams demonstrated that the majority of the data points (>70%) agreed with a magmatic origin, indicating a predominant magmatic source for the detrital zircons (Figure 12).

The identified age clusters within the zircons were approximately 2500 Ma, 2000–1800 Ma, 880 Ma, 820 Ma, 780 Ma, and 657–529 Ma. The principal peaks occurred around 880 Ma, 820 Ma, and 780 Ma. All four samples exhibited similar age peaks, reflecting a shared provenance.

In the Yangtze Block, one of China's three major Precambrian cratons, the crystalline basement, was predominantly obscured by Neoproterozoic-to-Mesozoic sedimentary layers, thus leaving the pre-Sinian basement rocks scarcely exposed. Zhen et al. [37] classified the ancient crustal materials in South China, which dated from the Paleoproterozoic to the Archean eras, into age groups corresponding to distinct periods of magmatic activity. The northern margin of the Yangtze Block hosts remnants of an Archean–Paleoproterozoic crystalline basement in the Yudongzi [38–44], Houhe [45], and Kongling complexes [46–51], one that spans various ages. Meanwhile, the zircon records of the Archean–Paleoproterozoic crystalline basement of the southern margin of the Yangtze Block are preserved within the Huili Group [52], Kunyang Group [53], Dongchuan Group [54], and Zuoke Complex in Yunnan [55,56]. These records provide crucial evidence for understanding the geological evolution of the Yangtze Block and its position within the broader tectonic framework of South China.

This geochronological dating identified eight older zircon grains, with $^{207}Pb/^{206}Pb$ ages bifurcating into two groups: approximately 2500 Ma and 2000–1800 Ma. The discoveries of detrital and inherited zircons from the Neoarchean to the Paleoproterozoic within the

Proterozoic sequences of the central and southern Yangtze Block were consistent with the previously documented Archean magmatic episodes [57–59]. These findings corroborate the region's protracted history of magmatic activities that span from the Archean through to the Paleoproterozoic era. This evidence lends support to the hypothesis of a substantial crystalline basement underlying the Yangtze Block during these epochs.

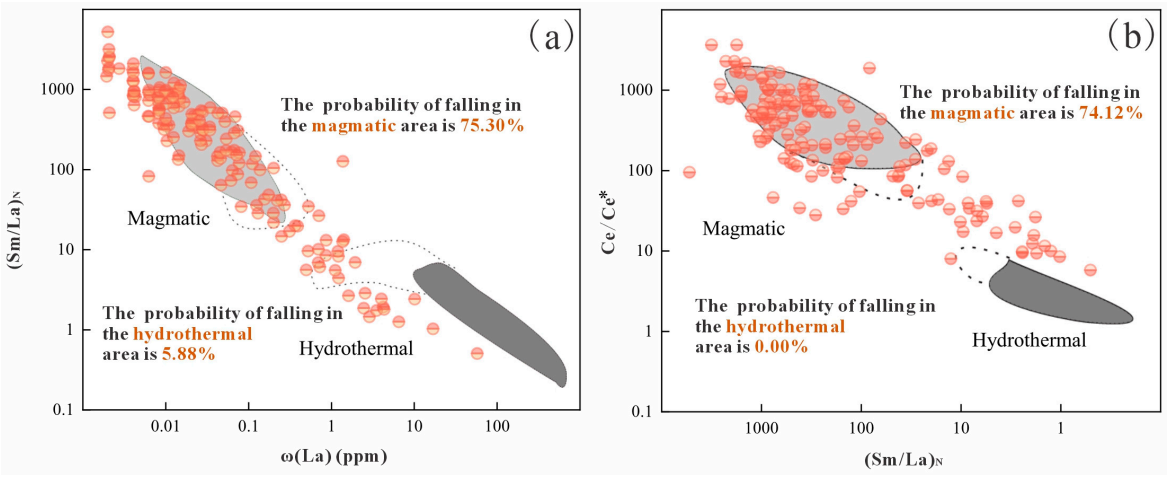

Figure 12. $(Sm/La)_N$ – ω(La) (**a**) and Ce/Ce* – $(Sm/La)_N$ (**b**) zircon genesis discrimination diagram. Both (**a**) and (**b**) are based on [60].

6.2. The Response of the Neoproterozoic Magmatic Events in the Kaiyang Region to the Splitting of the Rodinia Supercontinent

The concept of the Rodinia supercontinent, which is thought to have included most of the Earth's ancient landmasses, was first suggested by McMenamin [61], and it is believed to have existed during the Grenville orogeny spanning 1300–900 Ma [61–63]. Scholarly consensus suggests a timeline wherein Rodinia's amalgamation occurred between 1300–900 Ma, which was then succeeded by a series of breakup events commencing around 880–830 Ma with significant breakup events from 850–700 Ma, which could have possibly extended up to 600 Ma. These breakup phases were marked by assorted intensities of magmatism [62–65].

Regarding the position of the South China Craton in the Rodinia supercontinent, and the reasons for the large-scale breakup of Rodinia, the prevailing view among preceding researchers was that it was caused by a mantle superplume. This theory gained credence from the work of Li et al. [1], who correlated the genesis of the Jiangnan orogenic belt (~1000–960 Ma) with the global Grenville orogenic phase. The discovery of magmatic episodes between 830–795 Ma and 780–745 Ma within both the Rodinia supercontinent and the South China Craton lent support to the superplume model. This model suggests that the mantle plumes triggered lithospheric uplift, which, in a context of sustained extension and the thermal influence of mantle plumes, caused melting at the mantle–crust boundary, culminating in the fragmentation of Rodinia [66–69].

In contrast to this, there is the island arc model [70–72] and the plate rift valley model [73,74]. While the superplume model can account for the formation of basalts and some alkaline rocks, it does not fully explain the distribution of acidic–basic rocks in the Yangtze Block during the Neoproterozoic era [75]. The arc accretion model, although explanatory, cannot exclude the crustal contamination and later processes due to the geochemical characteristics influenced by various factors. The plate rift model, which is based primarily on studies of felsic magmatic rocks in the northeastern Jiangnan Orogen, deals with complex rock genesis and is not universally applicable in constraining tectonic settings.

Via integrating previous research, this study infers that the 880 Ma zircon age peak detected in the Kaiyang phosphorite-bearing rocks marks a period of intensified magmatic

activity, closely paralleling the global Grenville continental collision era (~1300–900 Ma). This denotes a localized response in South China at the culmination of the Grenville orogeny, and this served as the transition from Rodinia's assembly to its breakup stage. The ~820 Ma benchmark is perceived as the initiation of Rodinia's comprehensive fragmentation as it aligns with a peak in magmatic activities, which is emblematic of a prime zircon formation epoch due to widespread magmatic processes within and around the Yangtze Block [76]. The ~780 Ma demarcation signifies a critical phase in the breakup.

6.3. The Mineralization Age of Phosphate Deposits in the Doushantuo Formation, Kaiyang

The Doushantuo Formation, which is situated within the Qianzhong region, represents a crucial Precambrian stratigraphic unit, with its age determination being vital for defining the geological timeline and refining the stratigraphic framework of the central and southern margin of the Yangtze Block. Given the scarcity of identifiable fossil taxa from the Precambrian era, which hampers the delineation of fossil zones, dating detrital zircons within phosphorite sequences serves as an essential method for constraining the formation and mineralization timings of the strata [53,77]. While U-Pb zircon dating within interlayered tuff is the preferred method for age determination, the absence of such tuff layers necessitates the exploration of alternative dating proxies to accurately ascertain the chronological development of the strata. Comprehensive research conducted across different regions in South China employing various dating methods on distinct minerals within the Doushantuo Formation has helped establish its age. Initial studies by Xiao et al. [78], through a comparative analysis of global late Neoproterozoic strata, have suggested that the formation age of the regional Doushantuo phosphorite range between 600 and 550 Ma. Subsequent research has concurred that the genesis of the phosphorite began in the late Neoproterozoic, around 630 Ma [79,80].

In locations such as Hubei, Condon et al. [81] precisely determined the depositional timeframe of the Doushantuo Formation, anchoring it between 635.2 ± 0.57 Ma and 551.1 ± 0.7 Ma through the precise U-Pb zircon dating of interlayered tuff in Yichang. Liu et al. [82] further refined this timeline by acquiring a zircon U-Pb age of 614 ± 7.6 Ma from the Zhangcunping section in Yichang, which has contributed to the chronological delineation of the formation. Additionally, Zhu et al. [83] employed Re-Os dating on a bottom black shale within the formation in Hubei's Three Gorges area, securing an age of 591.1 ± 5.3 Ma. Zhou et al. [84] expanded upon these findings with a zircon U-Pb age of 609 ± 5 Ma from an upper phosphorite tuffaceous layer within the regional formation, while Yang et al. [85] derived ages of 587 ± 2.8 Ma and 587.5 ± 3.6 Ma from an Re-Os dating on black shale samples across different stratigraphic sections of the formation.

In Guizhou, a distinct set of age determinations was conducted by Barfod et al. [13], who, through Lu-Hf isotopic analyses of whole-rock samples from the Kaiyang phosphate mine, determined an age of 584 ± 26 Ma. Concurrently, Pb-Pb isochron dating of the upper ore layer at the Wengan phosphate mine yielded an age of 599.3 ± 4.2 Ma. Chen et al. [14,86] further contributed with Pb isochron ages of 572 ± 36 Ma and 576 ± 14 Ma from the upper ore layer phosphorites of the Wengan Doushantuo Formation. Shi [10] obtained Sm-Nd ages of 583 ± 19 Ma and Rb-Sr ages of 588 ± 8.6 Ma from the Wengan phosphate layers, and they delineated an Rb-Sr age of 582 ± 7.7 Ma on the Kaiyang phosphate strata. Hu et al. [87] acquired a Sm-Nd isochron age of 588 ± 35 Ma from the upper ore layer phosphorites at the Wengan site and an Rb-Sr isochron age of 596 ± 42 Ma for the Kaiyang mine, thus further enriching the temporal resolution of the Doushantuo Formation's age across these significant phosphorite-bearing regions.

In summary, discussions on the formation age of the Doushantuo Formation in Guizhou primarily focus on 600–540 Ma [11,13,86,87]. After the large-scale breakup of Rodinia, around 600 Ma, the Nanhua rift zone closed in the Qianzhong region, which became a passive continental margin with limited magmatic activity. The youngest zircons in the samples from the Kaiyang phosphorite-bearing rocks, aged 529 ± 22 Ma (PA770-7 basal sandstone) and 594 ± 9 Ma (MNW283-6 phosphorite), constrain the formation age

of the Doushantuo Formation in the Kaiyang area to 600 Ma–540 Ma, which aligns it with previous estimates for the Doushantuo Formation in Guizhou. Another group of younger zircons yielded ages of 651 ± 29 Ma (MNW283-6 phosphorite), 653 ± 24 Ma (PA797-2 top dolostone), and 657 ± 9 Ma (basal sandstone), with a weighted mean age of 654 Ma. Through a comparative analysis of the two youngest zircon ages, the CL image of the zircon from the basal sandstone, aged 529 Ma (sample PA770-7), exhibited uniformly distributed features typical of metamorphic zircon. Since the strata did not undergo extensive metamorphism after lithification, this zircon likely recorded the timing of pre-lithification metamorphic events. Combined with the minimum zircon age of 594 Ma from the phosphorite (sample MNW283-6), these findings collectively suggest that the formation of the Doushantuo Formation in Kaiyang occurred no earlier than 594 Ma, and it could have possibly even occurred after 529 Ma.

6.4. The Structural and Thermal Events after Phosphorite Mineralization in Kaiyang

The zircon fission-track (ZFT) partial annealing zone was delineated at 220 ± 40 °C, and it showcased variable annealing resistance across zircon grain populations. Zircon grains exposed to geological heat events exceeding 260 °C underwent a complete track erasure, while exposure to temperatures ranging from 180 °C to 260 °C led to partial track preservation, and those below 180 °C maintained intact tracks [88]. Therefore, ZFT ages serve as chronometers for thermal episodes that are potent enough to induce full annealing (>260 °C). They are often associated with regional tectonic activities and hydrothermal mineralization processes, and they are also often heralded by thermal anomalies. Employing ZFT dating can shed light on the thermal history, including cooling and uplift narratives, of the source terrain, as well as delineate the tectonic episodes encountered during the exhumation phase [89].

The thermal events experienced can reduce the annealing resistance of some zircons, thus leading to a dispersion in the recorded fission-track ages (Figure 13). These annealing influences are typically evident in tectonically active zones that have undergone multiple thermal incidents, suggesting multifaceted origins of the detrital zircons and their regulation by numerous thermal events [90]. The range of individual grain fission-track ages in basal sandstone sample PA283-10 and the top dolostone sample PA797-2, with certain grains recording ages predating the stratigraphic formation, illustrates the zircons' diverse provenance. The pooled ages obtained in this study (501 ± 30 Ma, 489 ± 25 Ma, and 366 ± 20 Ma) and the two distinct age groups (52–39 Ma) identified in a single sample are chronologically after the Doushantuo Formation's established age range. These findings highlight the occurrence of tectonic thermal events postdating the formation period within the studied area. The earlier ZFT ages (501 ± 30 Ma, 489 ± 25 Ma, and 366 ± 20 Ma) indicate that the region's strata underwent several uplift and exhumation episodes spanning from the Late Cambrian to the Late Devonian, thus intersecting with prominent tectonic episodes like the Duyun (480–450 Ma) and Guangxi (430–380 Ma) events.

These events accounted for the notable absence of Upper Ordovician and Upper Silurian strata in Guizhou, and they have prompted extensive east–west erosional activity, which was pivotal in sculpting the Qianzhong Uplift centered around Kaiyang [91]. Furthermore, the Yanshanian era (160–120 Ma) signified a peak in tectonic or magmatic activities in South China, with an escalation of extensional and rift-related tectonics during the later Yanshanian phase, which was likely propelled by significant Pacific plate interactions and led to extensive crustal extension in the region [92,93]. This orogeny redefined and augmented pre-existing tectonic frameworks in Guizhou, thus catalyzing the formation of numerous thrust and strike-slip faults [94].

The discerned age peaks of 52 Ma and 39 Ma in sample PA770-4 align with the Himalayan orogenic influences in central Guizhou (Figure 14) The Himalayan orogeny perpetuated the evolution and intensification of the regional tectonic fabric, and it is predominantly characterized by the reactivation of ancient faults and localized uplift dynamics. The Himalayan influence displayed a gradient from strong in the southeast to

weaker in the northwest, and this could be possibly attributed to the significant imprint of the Jiangnan Orogen toward the southeast. The observed disparity in ZFT ages between samples PA770-4 (53 ± 5 Ma, phosphorite) and PA770-7 (366 ± 19 Ma, basal sandstone), despite their identical stratigraphic horizons, may stem from variances in track annealing degrees that are influenced by proximity to active tectonic or magmatic hydrothermal heat sources alongside the intrinsic annealing attributes of the zircons, thus inducing variations in the recorded fission-track ages.

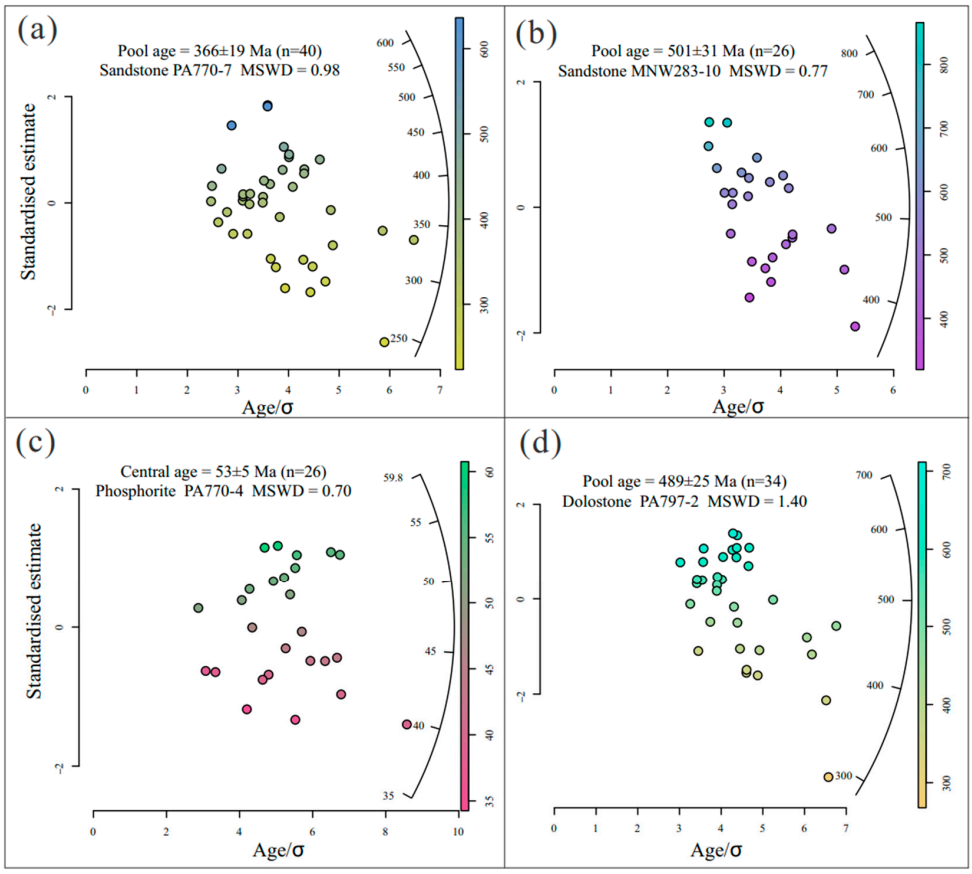

Figure 13. Kaiyang phosphorite-bearing rock single grain standard deviation and age variance radiograph: (**a**) Basal sandstone, PA770-7; (**b**) Basal sandstone, MNW283-10; (**c**) Phosphorite, PA770-4; (**d**) Top dolostone, PA797-2.

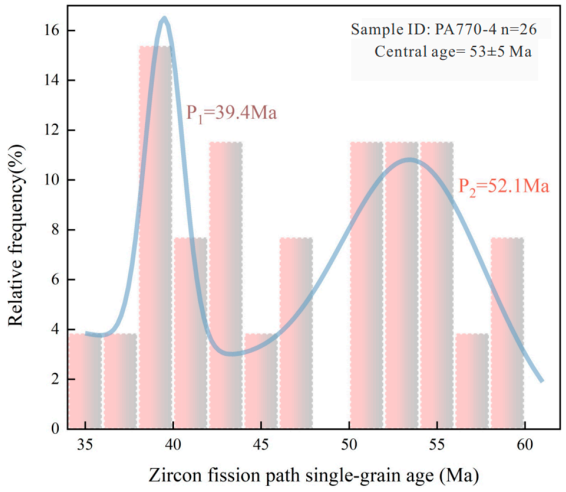

Figure 14. Kaiyang phosphorite sample PA770-4 zircon fission-track decomposition age chart.

7. Conclusions

Building upon comprehensive field investigations, this study examined the phosphorite-bearing Doushantuo Formation within the Kaiyang phosphate mining area located in the central and southern part of the Yangtze Block. Through detailed petrographical and whole-rock geochemical analyses, zircon U-Pb dating, and zircon fission-track low-temperature thermochronology, we arrived at several preliminary conclusions:

(1) The Doushantuo Formation in the Kaiyang area shows a stratigraphic sequence from top to bottom consisting of dolostone, phosphorite, and sandstone, with the primary mineral in the phosphorite being collophane, which contains P_2O_5 ranging from 30.1% to 34.8% and rare earth element contents between 117.01–266.55 ppm. The P_2O_5 content displays a significant positive correlation with the REE and Y elements, indicating that the rare earth elements are primarily hosted in collophane.

(2) The detrital zircons in the phosphorite-bearing rocks are predominantly of magmatic origin, with LA-ICP-MS U-Pb chronology indicating a major magmatic peak at ~820 Ma, followed by secondary peaks at ~2500 Ma, ~2000–1800 Ma, ~880 Ma, and ~780 Ma. These ages, in conjunction with previous studies, suggest that the oldest ages (~2500 Ma and ~2000–1800 Ma) provide direct evidence of a Paleoproterozoic crystalline basement in the central and southern of Yangtze Block. The Neoproterozoic ages correlate with the assembly (~880 Ma) and continued breakup (820–780 Ma) of the Rodinia supercontinent. The youngest zircon ages of the Doushantuo Formation in Kaiyang, at 594 $\pm$ 9 Ma and 529 $\pm$ 22 Ma, set a lower limit for the formation age of the phosphorite rocks, thus indicating they formed at least as late as 594 Ma (which is even later than 529 Ma).

(3) The zircon fission-track thermochronology, when integrated with previous research, indicated multiple episodes of tectonic uplift in the Kaiyang area after the formation of the phosphorite -bearing rocks. Magmatic events around 501–489 Ma and ~366 Ma are associated with the regional Caledonian movement, which culminated in the formation of the Qianzhong Uplift that is centered in Kaiyang. When dissecting earlier strata, the age range of 52–39 Ma was found to correspond to the Himalayan tectonic events in Guizhou, which resulted in the formation of numerous NNW-oriented folds.

Supplementary Materials: The following supporting information can be downloaded at: https://www.mdpi.com/article/10.3390/min14060585/s1, Table S1: Major element oxide content in samples (wt%, on whole-sample basis). Table S2: Trace element concentrations and rare earth element contents of the studied samples (ppm, on whole-sample basis). Table S3: Fission-track analytical results of the samples from kaiyang phosphorite-bearing rocks.

Author Contributions: Conceptualization, L.X. and Y.S.; formal analysis, Y.S. and T.L; investigation, L.X., Y.S., T.L., J.Z. and D.Z.; resources, L.X.; data curation, Y.S.; writing—original draft preparation, Y.S.; writing—review and editing, L.X. and Y.S. All authors have read and agreed to the published version of the manuscript.

Funding: This research was funded by the National Key R&D Program of China (grant number 2021YFC2901703).

Data Availability Statement: The original contributions presented in this study are included in the article.

Acknowledgments: We are grateful to the anonymous reviewers for their valuable suggestions in improving the manuscript. We are also grateful to Dai Zuowen, Chen Ziyuan, and Zhong Zhenyu for their assistance in the field sampling.

Conflicts of Interest: The authors declare no conflicts of interest.

References

1. Li, X.H.; Li, Z.X.; Ge, W.C.; Zhou, H.W.; Li, W.X.; Liu, Y.; Wingate, M. Neoproterozoic granitoids in South China: Crustal melting above a mantle plume at ca. 825 Ma? *Precambrian Res.* **2003**, *122*, 45–83. [CrossRef]
2. Wang, J.; Li, Z.X. History of Neoproterozoic rift basins in South China: Implications for Rodinia Break-up. *Precambrian Res.* **2003**, *122*, 141–158. [CrossRef]
3. Jiang, X.S.; Wang, J.; Cui, X.Z.; Zhuo, J.W.; Xiong, G.Q.; Lu, J.Z.; Liu, J.H. Zircon SHRIMP U-Pb geochronology of the Neoproterozoic Chengjiang Formation in central Yunnan Province (SW China) and its geological significance. *Sci. China Earth Sci.* **2012**, *55*, 1815–1826. [CrossRef]
4. Pan, G.T.; Xiao, Q.H.; Lu, S.N.; Deng, J.F.; Feng, Y.M.; Zhang, K.X.; Zhang, Z.Y.; Wang, F.G.; Xing, G.F.; Hao, G.J.; et al. Subdivision of tectonic units in China. *Geol. China* **2009**, *36*, 1–28. (In Chinese)
5. Wang, L.J.; Zhang, K.X.; Lin, S.F.; He, W.H.; Kou, X.H.; Xiao, H.Z. Turbidite record of a Neoproterozoic active continental margin in the West Cathaysia terrane, South China: Implications for the relationships between the Yangtze and Cathaysia blocks and their positions in Rodinia. *Precambrian Res.* **2019**, *337*, 105457. [CrossRef]
6. Zou, H.; Li, Q.L.; Bagas, L.; Wang, X.C.; Chen, A.Q.; Li, X.H. A Neoproterozoic low-$\delta^{18}O$ magmatic ring around South China: Implications for configuration and breakup of Rodinia supercontinent. *Earth Planet. Sci. Lett.* **2021**, *575*, 117196. [CrossRef]
7. Huang, C.C.; Zou, H.; Bagas, L.; Chen, H.F.; Xiao, B.; Jiang, X.W.; Li, M.; Hu, C.H.; Yu, L.M. Mid-Neoproterozoic tectonic evolution of the northern margin of the Yangtze Block, South China: New insights from high-temperature magma events. *Lithos* **2022**, *420–421*, 106711. [CrossRef]
8. Kennedy, M.J.; Runnegar, B.; Prave, A.R.; Hoffmann, K.H.; Arthur, M.A. Two or four Neoproterozoic glaciations? *Geology* **1998**, *26*, 1059–1063. [CrossRef]
9. Hoffman, P.F.; Abbot, D.S.; Ashkenazy, Y.; Benn, D.; Brocks, J.; Cohen, P.; Cox, G.; Creveling, J.; Donnadieu, Y.; Erwin, D.; et al. Snowball earth climate dynamics and Cryogenian geology-geobiology. *Sci. Adv.* **2017**, *3*, e1600983. [CrossRef]
10. Shi, C.H. Formation of Phosphorite Deposit, Break-Up of Rodinia Supercontinent and Biology Explosion—A Case Study of Wengan, Kaiyang and Zhijin Phosphorite Deposits of Guizhou Province. Ph.D. Thesis, Institute of Geochemistry, Chinese Academy of Science, Guiyang, China, 2005. (In Chinese).
11. Knoll, A.H.; Xiao, S.H. On the age of the Doushantuo Formation. *Acta Micropalaeontol. Sin.* **1999**, *16*, 225–236.
12. McDougall, I.; Harrison, T.M. *Geochronology and Thermochronology by the $^{40}Ar/^{39}Ar$ Method*; Oxford University Press: Oxford, UK, 1999. [CrossRef]
13. Barfod, G.; Albarède, F.; Knoll, A.; Xiao, S.H.; Frei, R.; Baker, J. Implications for the Neoproterozoic Biological and Climatic History from Dating of the Doushantuo Phosphorites, S. China. *AGU Fall Meet. Abstr.* **2002**, *1*, B71B-0737.
14. Chen, D.F.; Dong, W.; Zhu, B.; Chen, X. Pb-Pb ages of Neoproterozoic Doushantuo phosphorites in South China: Constraints on early metazoan evolution and glaciation events. *Precambrian Res.* **2004**, *132*, 123–132. [CrossRef]
15. Chew, D.M.; Spikings, R.A. Geochronology and Thermochronology Using Apatite: Time and Temperature, Lower Crust to Surface. *Elements* **2015**, *11*, 189–194. [CrossRef]
16. Hawkesworth, C.; Kemp, A.I.S. Using hafnium and oxygen isotopes in zircons to unravel the record of crustal evolution. *Chem. Geol.* **2006**, *226*, 144–162. [CrossRef]
17. Kemp, A.I.S.; Wilde, S.; Hawkesworth, C.; Coath, C.D.; Nemchin, A.; Pidgeon, R.; Vervoort, J.; Dufrane, S.A. Hadean crustal evolution revisited: New constraints from Pb–Hf isotope systematics of the Jack Hills zircons. *Earth Planet. Sci. Lett.* **2010**, *296*, 45–56. [CrossRef]
18. Wang, H.S.; Cai, X.L.; Lei, L.F. Analysis on structural characteristics in Yangshui mining area of Kaiyang phosphate Mine, Central Guizhou. *Geol. Chem. Miner.* **2017**, *39*, 90–95. (In Chinese)
19. Wang, Z.P.; Zhang, Y.G.; Du, Y.S.; Chen, G.Y.; Liu, J.Z.; Xu, Y.Y.; Tan, D.W.; Li, L.; Wang, D.F.; Wu, W.M. Reconstruction of quantitative lithofacies palaeogeography of the Sinian Doushantuo Age of phosphorite depositional zone in Kaiyang area, central Guizhou Province. *J. Palaeogeogr. (Chin. Ed.)* **2016**, *18*, 399–410. (In Chinese)
20. Siivola, J.; Schmid, R. Recommendations by the IUGS Subcommission on the Systematics of Metamorphic Rocks: Web version 01.02.07. *Geology* **2007**.
21. Vermeesch, P. IsoplotR: A free and open toolbox for geochronology. *Geosci. Front.* **2018**, *9*, 1479–1493. [CrossRef]
22. Hurford, A.J. Standardization of fission track dating calibration: Recommendation by the Fission Track Working Group of the I.U.G.S. Subcommission on Geochronology. *Chem. Geol. Isot. Geosci. Sect.* **1990**, *80*, 171–178. [CrossRef]
23. Galbraith, R.F. On statistical models for fission track counts. *J. Int. Assoc. Math. Geol.* **1981**, *13*, 471–478. [CrossRef]
24. Brandon, M.T. Decomposition of fission-track grain-age distributions. *Am. J. Sci.* **1992**, *292*, 535–564. [CrossRef]
25. Rudnick, R.; Gao, S. Composition of the Continental Crust. *Treatise Geochem.* **2003**, *3*, 1–64. [CrossRef]
26. Mclennan, S.M. Rare earth elements in sedimentary rocks: Influence of provenance and sedimentary processes. *Rev. Mineral. Geochem.* **1989**, *21*, 169–200.
27. Sun, S.S.; Mcdonough, W.F. Chemical and isotopic systematics of ocean basalts: Implications for mantle composition and processes, in Magmatism in the Ocean Basins. *Geol. Soc. Lond. Spec. Publ.* **1989**, *423*, 13–345.
28. Watson, E.B.; Wark, D.A.; Thomas, J.B. Crystallization thermometers for zircon and rutile. *Contrib. Mineral. Petrol.* **2006**, *151*, 413. [CrossRef]

29. Green, P.F.; Duddy, I.R.; Laslett, G.M.; Hegarty, K.A.; Gleadow, A.J.W.; Lovering, J.F. Thermal annealing of fission tracks in apatite 4. Quantitative modelling techniques and extension to geological timescales. *Chem. Geol. Isot. Geosci. Sect.* **1989**, *79*, 155–182. [CrossRef]
30. McDannell, K.T. Notes on statistical age dispersion in fission-track datasets: The chi-square test, annealing variability, and analytical considerations. *EarthArXiv* **2020**, *1–4*. [CrossRef]
31. Galbraith, R.F.; Laslett, G.M. Statistical models for mixed fission track ages. *Nucl. Tracks Radiat. Meas.* **1993**, *21*, 459–470. [CrossRef]
32. Gehrels, G. Detrital Zircon U-Pb Geochronology Applied to Tectonics. *Annu. Rev. Earth Planet. Sci.* **2014**, *42*, 127–149. [CrossRef]
33. Olierook, H.; Jourdan, F.; Merle, R. Age of the Barremian–Aptian boundary and onset of the Cretaceous Normal Superchron. *Earth-Sci. Rev.* **2019**, *197*, 102906. [CrossRef]
34. Rubatto, D. Zircon: The Metamorphic Mineral. *Rev. Mineral. Geochem.* **2017**, *83*, 261–295. [CrossRef]
35. Hoskin, P.W.O.; Schaltegger, U. The Composition of Zircon and Igneous and Metamorphic Petrogenesis. *Rev. Mineral. Geochem.* **2003**, *53*, 27–62. [CrossRef]
36. Li, C.M. A Review on the Minerageny and Situ Microanalytical Dating Techniques of Zircons. *North China Geol.* **2009**, *32*, 161–174. (In Chinese)
37. Zheng, Y.F.; Zhang, S.B. Formation and evolution of Precambrian continental crust in South China. *Chin. Sci. Bull.* **2007**, *52*, 1–12. [CrossRef]
38. Sun, M.; Chen, N.S.; Zhao, G.C.; Wilde, S.; Ye, K.; Guo, J.H.; Chen, Y.; Yuan, C. U-Pb zircon and Sm-Nd isotopic study of the Huangtuling granulite, Dabie-Sulu belt, China: Implication for the paleoproterozoic tectonic history of the Yangtze Craton. *Am. J. Sci.* **2008**, *308*, 469–483. [CrossRef]
39. Zhang, L.J.; Ma, C.Q.; Wang, L.X.; She, Z.B.; Wang, S.M. Discovery of Paleoproterozoic rapakivi granite on the northern margin of the Yangtze block and its geological significance. *Chin. Sci. Bull.* **2011**, *56*, 306–318. [CrossRef]
40. Wu, Y.B.; Gao, S.; Zhang, H.F.; Zheng, J.P.; Liu, X.C.; Wang, H.; Gong, H.J.; Zhou, L.; Yuan, H.L. Geochemistry and zircon U–Pb geochronology of Paleoproterozoic arc related granitoid in the Northwestern Yangtze Block and its geological implications. *Precambrian Res.* **2012**, *200–203*, 26–37. [CrossRef]
41. Chen, K.; Gao, S.; Wu, Y.B.; Guo, J.L.; Hu, Z.C.; Liu, Y.S.; Zong, K.Q.; Liang, Z.W.; Geng, X.L. 2.6–2.7 Ga crustal growth in Yangtze craton, South China. *Precambrian Res.* **2013**, *224*, 472–490. [CrossRef]
42. Wu, Y.B.; Zhou, G.Y.; Gao, S.; Liu, X.C.; Qin, Z.W.; Wang, H.; Yang, J.Z.; Yang, S.H. Petrogenesis of Neoarchean TTG rocks in the Yangtze Craton and its implication for the formation of Archean TTGs. *Precambrian Res.* **2014**, *254*, 73–86. [CrossRef]
43. Hui, B.; Dong, Y.P.; Cheng, C.; Long, X.P.; Liu, X.M.; Yang, Z.; Sun, S.S.; Zhang, F.F.; Varga, J. Zircon U–Pb chronology, Hf isotope analysis and whole-rock geochemistry for the Neoarchean-Paleoproterozoic Yudongzi complex, northwestern margin of the Yangtze craton, China. *Precambrian Res.* **2017**, *301*, 65–85. [CrossRef]
44. Chen, Q.; Sun, M.; Zhao, G.C.; Zhao, J.H.; Zhu, W.L.; Long, X.P.; Wang, J. Episodic crustal growth and reworking of the Yudongzi terrane, South China: Constraints from the Archean TTGs and potassic granites and Paleoproterozoic amphibolites. *Lithos* **2019**, *326–327*, 1–18. [CrossRef]
45. Lin, W.L.; Gao, S.; Zhang, B.R.; Zhou, L.; Zhang, H.F. Early Precambrian crustal evolution at the northern margin of the Yangtze Craton—Element and isotope geochemical constraints of the Houhe Complex. *Mineral. Petrol.* **1997**, *4*, 27–33. (In Chinese) [CrossRef]
46. Qiu, Y.M.; Gao, S.; McNaughton, N.J.; Groves, D.I.; Ling, W.L. First evidence of >3.2 Ga continental crust in the Yangtze craton of south China and its implications for Archean crustal evolution and Phanerozoic tectonics. *Geology* **2000**, *28*, 11–14. [CrossRef]
47. Qiu, X.F.; Zhao, X.; Yang, H.R.; Wei, Y.; Wu, N.; Lu, S.; Jang, T.; Peng, L. Paleoproterozoic metamorphic event in the nucleus of the Yangtze craton: Evidence from U-Pb geochronology of the metamorphic zircons from the khondalite. *Geol. Bull. China* **2017**, *36*, 706–714.
48. Wu, Y.B.; Gao, S.; Zhang, H.F.; Yang, S.H.; Liu, X.C.; Jiao, W.F.; Liu, Y.S.; Yuan, H.L.; Gong, H.J.; He, M.C. U-Pb age, trace-element, and Hf-isotope compositions of zircon in a quartz vein from eclogite in the western Dabie Mountains: Constraints on fluid flow during early exhumation of ultrahigh-pressure rocks. *Am. Mineral.* **2009**, *94*, 303–312. [CrossRef]
49. Jiao, W.F.; Wu, Y.B.; Yang, S.H.; Peng, M.; Wang, J. The oldest basement rock in the Yangtze Craton revealed by zircon U-Pb age and Hf isotope composition. *Sci. China Ser. D Earth Sci.* **2009**, *52*, 1393–1399. [CrossRef]
50. Guo, J.L.; Gao, S.; Wu, Y.B.; Li, M.; Chen, K.; Hu, Z.C.; Liang, Z.W.; Liu, Y.S.; Zhou, L.; Zong, K.Q.; et al. 3.45 Ga granitic gneisses from the Yangtze Craton, South China: Implications for Early Archean crustal growth. *Precambrian Res.* **2014**, *242*, 82–95. [CrossRef]
51. Han, Q.S.; Peng, S.B.; Polat, A.; Kusky, T.; Deng, H.; Wu, T.Y. A ca.2.1 Ga Andean-type margin built on metasomatized lithosphere in the northern Yangtze craton, China: Evidence from high-Mg basalts and andesites. *Precambrian Res.* **2018**, *309*, 309–324. [CrossRef]
52. Liu, H.Y.; Xia, B.; Zhang, Y.Q. The study presents the SHRIMP dating of zircon from the Na-rich alkaline rocks in Maomao Gully, Panxi, Huali, and discusses its geological significance. *Chin. Sci. Bull.* **2004**, *49*, 1431–1438. (In Chinese)
53. Sun, W.H.; Zhou, M.F.; Gao, J.F.; Yang, Y.H.; Zhao, X.F.; Zhao, J.H. Detrital zircon U–Pb geochronological and Lu–Hf isotopic constraints on the Precambrian magmatic and crustal evolution of the western Yangtze Block, SW China. *Precambrian Res.* **2009**, *172*, 99–126. [CrossRef]

54. Zhao, X.F.; Zhou, M.F.; Li, J.W.; Sun, M.; Gao, J.F.; Sun, W.H.; Yang, J.H. Late Paleoproterozoic to early Mesoproterozoic Dongchuan Group in Yunnan, SW China: Implications for tectonic evolution of the Yangtze Block. *Precambrian Res.* **2010**, *182*, 57–69. [CrossRef]
55. Zhao, T.Y.; Li, J.; Liu, G.C.; Cawood, P.A.; Zi, J.W.; Wang, K.; Feng, Q.L.; Hu, S.B.; Zeng, W.T.; Zhang, H. Petrogenesis of Archean TTGs and potassic granites in the southern Yangtze Block: Constraints on the early formation of the Yangtze Block. *Precambrian Res.* **2020**, *347*, 105848. [CrossRef]
56. Cui, X.Z.; Wang, J.; Wang, X.C.; Wilde, S.A.; Ren, G.M.; Li, S.J.; Deng, Q.; Ren, F.; Liu, J.P. Early crustal evolution of the Yangtze Block: Constraints from zircon U-Pb-Hf isotope systematics of 3.1–1.9 Ga granitoids in the Cuoke Complex, SW China. *Precambrian Res.* **2021**, *357*, 106155. [CrossRef]
57. Greentree, M.R.; Li, Z.X. The oldest known rocks in south–western China: SHRIMP U–Pb magmatic crystallisation age and detrital provenance analysis of the Paleoproterozoic Dahongshan Group. *J. Asian Earth Sci.* **2008**, *33*, 289–302. [CrossRef]
58. Wang, L.J.; Yu, J.H.; Griffin, W.L.; O'Reilly, S.Y. Early crustal evolution in the western Yangtze Block: Evidence from U–Pb and Lu–Hf isotopes on detrital zircons from sedimentary rocks. *Precambrian Res.* **2012**, *222–223*, 368–385. [CrossRef]
59. Chen, W.T.; Zhou, M.F.; Zhao, X.F. Late Paleoproterozoic sedimentary and mafic rocks in the Hekou area, SW China: Implication for the reconstruction of the Yangtze Block in Columbia. *Precambrian Res.* **2013**, *231*, 61–77. [CrossRef]
60. Hoskin, P.W.O. Trace-element composition of hydrothermal zircon and the alteration of Hadean zircon from the Jack Hills, Australia. *Geochim. Et Cosmochim. Acta* **2005**, *69*, 637–648. [CrossRef]
61. McMenamin, M.A.S.; McMenamin, D.L.S. *The Emergence of Animals the Cambrian Breakthrough*; Columbia University Press: New York, NY, USA, 1990.
62. Moores, E.M. Southwest U.S.-East Antarctic (SWEAT) connection: A hypothesis. *Geology* **1991**, *19*, 425–428. [CrossRef]
63. Hoffman, P.F. Did the Breakout of Laurentia Turn Gondwanaland Inside-Out? *Science* **1991**, *252*, 1409–1412. [CrossRef]
64. Wang, X.L.; Zhou, J.C.; Griffin, W.L.; Wang, R.C.; Qiu, J.S.; O'Reilly, S.Y.; Xu, X.S.; Liu, X.M.; Zhang, G.L. Detrital zircon geochronology of Precambrian basement sequences in the Jiangnan orogen: Dating the assembly of the Yangtze and Cathaysia Blocks. *Precambrian Res.* **2007**, *159*, 117–131. [CrossRef]
65. Sun, L.; Wang, W.; Pandit, M.K.; Lu, G.M.; Xue, E.K.; Huang, B.; Zhang, Y.; Jin, W.; Tian, Y. Geochemical and detrital zircon age constraints on Meso- to Neoproterozoic sedimentary basins in the southern Yangtze Block: Implications on Proterozoic geodynamics of South China and Rodinia configuration. *Precambrian Res.* **2022**, *378*, 106779. [CrossRef]
66. Ling, W.L.; Gao, S.; Zhang, B.R.; Li, H.M.; Liu, Y.; Cheng, J.P. Neoproterozoic tectonic evolution of the northwestern Yangtze craton, South China: Implications for amalgamation and break-up of the Rodinia Supercontinent. *Precambrian Res.* **2003**, *122*, 111–140. [CrossRef]
67. Sun, L.; Wang, W.; Lu, G.M.; Xue, E.K.; Huang, S.F.; Pandit, M.K.; Huang, B.; Tong, X.R.; Tian, Y.; Zhang, Y. Neoproterozoic geodynamics of South China and implications on the Rodinia configuration: The Kunyang Group revisited. *Precambrian Res.* **2021**, *363*, 106338. [CrossRef]
68. Zhu, W.G.; Zhong, H.; Li, X.H.; Deng, H.L.; He, D.F.; Wu, K.W.; Bai, Z.J. SHRIMP zircon U–Pb geochronology, elemental, and Nd isotopic geochemistry of the Neoproterozoic mafic dykes in the Yanbian area, SW China. *Precambrian Res.* **2008**, *164*, 66–85. [CrossRef]
69. Huang, X.L.; Xu, Y.G.; Li, X.H.; Li, W.X.; Lan, J.B.; Zhang, H.H.; Liu, Y.S.; Wang, Y.B.; Li, H.Y.; Luo, Z.Y.; et al. Petrogenesis and tectonic implications of Neoproterozoic, highly fractionated A-type granites from Mianning, South China. *Precambrian Res.* **2008**, *165*, 190–204. [CrossRef]
70. Zhou, M.F.; Kennedy, A.; Sun, M.; Malpas, J.; Lesher, M. Neoproterozoic Arc-Related Mafic Intrusions along the Northern Margin of South China: Implications for the Accretion of Rodinia. *J. Geol.* **2002**, *110*, 611–618. [CrossRef]
71. Zhao, J.H.; Zhou, M.F.; Yan, D.P.; Zheng, J.P.; Li, J.W. Reappraisal of the ages of Neoproterozoic strata in South China: No connection with the Grenvillian orogeny. *Geology* **2011**, *39*, 299–302. [CrossRef]
72. Wang, Y.J.; Zhang, A.M.; Cawood, P.A.; Fan, W.M.; Xu, J.F.; Zhang, G.W.; Zhang, Y.Z. Geochronological, geochemical and Nd–Hf–Os isotopic fingerprinting of an early Neoproterozoic arc–back-arc system in South China and its accretionary assembly along the margin of Rodinia. *Precambrian Res.* **2013**, *231*, 343–371. [CrossRef]
73. Zheng, Y.F.; Zhang, S.B.; Zhao, Z.F.; Wu, Y.B.; Li, X.H.; Li, Z.X.; Wu, F.Y. Contrasting zircon Hf and O isotopes in the two episodes of Neoproterozoic granitoids in South China: Implications for growth and reworking of continental crust. *Lithos* **2007**, *96*, 127–150. [CrossRef]
74. Zheng, Y.F.; Wu, R.X.; Wu, Y.B.; Zhang, S.B.; Yuan, H.L.; Wu, F.Y. Rift melting of juvenile arc-derived crust: Geochemical evidence from Neoproterozoic volcanic and granitic rocks in the Jiangnan Orogen, South China. *Precambrian Res.* **2008**, *163*, 351–383. [CrossRef]
75. Cui, X.Z.; Jiang, X.S.; Wang, J.; Zhuo, J.W.; Jiang, Z.F.; Wu, H.; Deng, Q.; Wei, Y.N. New evidence for the formation age of basalts from the lowermost Chengjiang formation in the western Yangtze block and its geological implications. *Acta Petrol. Et Mineral.* **2015**, *34*, 1–13. (In Chinese)
76. Dong, S.W.; Zhang, Y.S.; Gao, R.; Su, J.B.; Liu, M.; Li, J.H. A possible buried Paleoproterozoic collisional orogen beneath central South China: Evidence from seismic-reflection profiling. *Precambrian Res.* **2015**, *264*, 1–10. [CrossRef]
77. Spencer, C.; Kirkland, C.; Taylor, R. Strategies towards statistically robust interpretations of in situ U–Pb zircon geochronology. *Geosci. Front.* **2015**, *7*, 581–589. [CrossRef]

78. Xiao, S.H.; Knoll, A.H.; Yuan, X.L. Morphological reconstruction of Miaohephyton bifurcatum, a possible brown alga from the Neoproterozoic Doushantuo Formation, South China. *J. Paleontol.* **1998**, *72*, 1072–1086. [CrossRef]
79. Reinhard, C.T.; Planavsky, N.J.; Gill, B.C.; Ozaki, K.; Robbins, L.J.; Lyons, T.W.; Fischer, W.W.; Wang, C.J.; Cole, D.B.; Konhauser, K.O. Evolution of the global phosphorus cycle. *Nature* **2017**, *541*, 386–389. [CrossRef]
80. Cox, G.M.; Lyons, T.W.; Mitchell, R.N.; Hasterok, D.; Gard, M. Linking the rise of atmospheric oxygen to growth in the continental phosphorite inventory. *Earth Planet. Sci. Lett.* **2018**, *489*, 28–36. [CrossRef]
81. Condon, D.; Zhu, M.Y.; Bowring, S.; Wang, W.; Yang, A.H.; Jin, Y.G. U-Pb Ages from the Neoproterozoic Doushantuo Formation, China. *Science* **2005**, *308*, 95–98. [CrossRef]
82. Liu, P.J.; Yin, C.Y.; Gao, L.Z.; Tang, F.; Chen, S.M. New material of microfossils from the Ediacaran Doushantuo Formation in the Zhangcunping area, Yichang, Hubei Province and its zircon SHRIMP U-Pb age. *Chin. Sci. Bull.* **2009**, *54*, 1058–1064. [CrossRef]
83. Zhu, B.; Becker, H.; Jiang, S.Y.; Pi, D.H.; Fischer Gödde, M.; Yang, J.H. Re–Os geochronology of black shales from the Neoproterozoic Doushantuo Formation, Yangtze platform, South China. *Precambrian Res.* **2013**, *225*, 67–76. [CrossRef]
84. Zhou, C.M.; Li, X.H.; Xiao, S.H.; Lan, Z.W.; Ouyang, Q.; Guan, C.G.; Chen, Z.H.E. A new SIMS zircon U–Pb date from the Ediacaran Doushantuo Formation: Age constraint on the Weng'an biota. *Geol. Mag.* **2017**, *154*, 1193–1201. [CrossRef]
85. Yang, C.; Rooney, A.D.; Condon, D.J.; Li, X.H.; Grazhdankin, D.V.; Bowyer, F.T.; Hu, C.L.; Macdonald, F.A.; Zhu, M.Y. The tempo of Ediacaran evolution. *Sci. Adv.* **2021**, *7*, eabi9643. [CrossRef]
86. Chen, Y.Q.; Jiang, S.Y.; Ling, H.F.; Yang, J.H. Pb–Pb dating of black shales from the Lower Cambrian and Neoproterozoic strata, South China. *Geochemistry* **2009**, *69*, 183–189. [CrossRef]
87. Hu, R.Z.; Peng, J.T.; Ma, D.S.; Su, W.C.; Shi, C.H.; Bi, X.W.; Tu, G.C. Epoch of large-scale low temperature mineralizations in southwestern Yangtze massif. *Miner. Depos.* **2007**, *6*, 583–596. (In Chinese)
88. Brandon, M.T.; Roden Tice, M.K.; Garver, J.I. Late Cenozoic exhumation of the Cascadia accretionary wedge in the Olympic Mountains, northwest Washington State. *GSA Bull.* **1998**, *110*, 985–1009. [CrossRef]
89. Wang, Y.D.; Zheng, J.J.; Zhang, W.L.; Li, S.Y.; Liu, X.W.; Yang, X.; Liu, Y.H. Cenozoic uplift of the Tibetan Plateau: Evidence from the tectonic–sedimentary evolution of the western Qaidam Basin. *Geosci. Front.* **2012**, *3*, 175–187. [CrossRef]
90. Shi, G.Z.; Soares, C.J.; Shen, C.B.; Wang, H.; Yang, C.Q.; Liang, C.; Liu, M.H. Combined detrital zircon fission track and U-Pb dating of the Late Paleozoic to Early Mesozoic sandstones in the Helanshan, western Ordos fold-thrust belt: Constraints for provenance and exhumation history. *J. Geodyn.* **2019**, *130*, 57–71. [CrossRef]
91. Qiu, L.; Yan, D.P.; Zhou, M.F.; Gao, J.F.; Tang, S.L.; Barnes, M. Geochemistry and U-Pb zircon age of Late Triassic volcanogenic sediments in the central Yangtze Block: Origin and tectonic implications. *Neues Jahrb. Für Mineral. Abh. J. Mineral. Geochem.* **2015**, *192*, 211–227. [CrossRef]
92. Wang, Y.J.; Fan, W.M.; Cawood, P.; Ji, S.C.; Peng, T.P.; Chen, X.Y. Indosinian high-strain deformation for the Yunkaidashan tectonic belt, south China: Kinematics and $^{40}Ar/^{39}Ar$ geochronological constraints. *Tectonics* **2007**, *26*, TC6008. [CrossRef]
93. Wang, J.L.; Lin, F.C.; Hou, L.; Zhang, J.R.; Peng, Z.; Zhu, S.B.; Wu, S.Y. Characteristics and metallogenic significance of fluid inclusions in the Nibao gold deposit, Guizhou. *Bull. Mineral. Petrol. Geochem.* **2014**, *33*, 688–699. (In Chinese) [CrossRef]
94. Yang, K.G.; Li, X.G.; Dai, C.G. Superimposition deformation controlled and adjusted by faults: An example from Yanshanian structural deformation in Guizhou province. *Bull. Geol. Sci. Technol.* **2012**, *31*, 50–56. (In Chinese)